

# ResViT: Residual vision transformers for multi-modal medical image synthesis

Onat Dalmaz, Mahmut Yurt, and Tolga Çukur

**Abstract**—Multi-modal imaging is a key healthcare technology that is often underutilized due to costs associated with multiple separate scans. This limitation yields the need for synthesis of unacquired modalities from the subset of available modalities. In recent years, generative adversarial network (GAN) models with superior depiction of structural details have been established as state-of-the-art in numerous medical image synthesis tasks. GANs are characteristically based on convolutional neural network (CNN) backbones that perform local processing with compact filters. This inductive bias in turn compromises learning of contextual features. Here, we propose a novel generative adversarial approach for medical image synthesis, ResViT, to combine local precision of convolution operators with contextual sensitivity of vision transformers. ResViT employs a central bottleneck comprising novel aggregated residual transformer (ART) blocks that synergistically combine convolutional and transformer modules. Comprehensive demonstrations are performed for synthesizing missing sequences in multi-contrast MRI, and CT images from MRI. Our results indicate superiority of ResViT against competing methods in terms of qualitative observations and quantitative metrics.

**Index Terms**—medical image synthesis, transformer, residual, vision, adversarial, generative, unified

## I. INTRODUCTION

Medical imaging plays a pivotal role in modern healthcare by enabling in vivo examination of pathology in the human body. In many clinical scenarios, multi-modal protocols are desirable that involve a diverse collection of images from multiple scanners (e.g., CT, MRI) [1], or multiple acquisitions from a single scanner (multi-contrast MRI) [2]. Complementary information about tissue morphology, in turn, empower physicians to diagnose with higher accuracy and confidence. Unfortunately, numerous factors including uncooperative patients and excessive scan times prohibit ubiquitous multi-modal imaging [3], [4]. As a result, there has been ever-growing interest in synthesizing unacquired images in multi-modal protocols from the subset of available images, bypassing costs associated with additional scans [5], [6].

Medical image synthesis aims to predict target-modality images for a subject given source-modality images acquired under a limited scan budget [7]. This is an ill-posed inverse problem since medical images are high dimensional, target-modality data are absent during inference, and there exist

nonlinear differences in tissue contrast across modalities [8]–[13]. Unsurprisingly, recent adoption of deep learning methods for solving this difficult problem has enabled major performance leaps [14]–[21]. In learning-based synthesis, network models effectively capture a prior on the joint distribution of source-target images [22]–[24]. Earlier studies using CNNs for this purpose reported significant improvements over traditional approaches [22], [23], [25]–[28]. GANs were later introduced that leverage an adversarial loss to increase capture of detailed tissue structure [24], [29]–[35]. Further improvements were attained by leveraging enhanced architectural designs [36]–[39], and learning strategies [40]–[42].

Despite their prowess, prior learning-based synthesis models are fundamentally based on convolutional architectures that use compact filters to extract local image features [43], [44]. Exploiting correlations among neighboring image pixels, this inductive bias reduces the number of model parameters to facilitate learning. However, it also limits expressiveness for contextual features that reflect long-range spatial dependencies [45], [46]. Indeed, spatially distant voxels in medical images can show strong correlations especially when they belong to the same tissue. For instance, bone tissue in the skull or CSF in the ventricles broadly distribute over large image regions, whether spatially contiguous or segregated. In principle, synthesis can be enhanced by priors that capture interactions among distant pixels. While emergent transformer architectures in computer vision forego convolution in favor of global attention operators [47], adoption of vanilla transformers in tasks with pixel-level outputs is challenging due to computational burden and limited localization abilities [48].

Here, we propose a novel deep learning model for medical image synthesis, ResViT, that combines the sensitivity of vision transformers to global context, the localization power of CNNs, and the realism of adversarial learning. ResViT’s generator follows an encoder-decoder architecture with a central bottleneck to distill task-critical information. The encoder and decoder comprise residual CNN blocks to leverage local precision of convolution operators [49]. The bottleneck comprises novel aggregated residual transformer (ART) blocks to synergistically preserve local and global context, with a weight-sharing strategy to minimize model complexity. To improve practical utility, a unified ResViT implementation is introduced that consolidates models for numerous source-target configurations. Demonstrations are performed for synthesizing missing sequences in multi-contrast MRI, and CT from MRI. Comprehensive experiments on imaging datasets from healthy subjects and patients clearly indicate the superiority of the proposed method against competing methods.

This study was supported in part by a TUBA GEBIP 2015 fellowship, and a BAGEP 2017 fellowship (Corresponding author: Tolga Çukur).

Onat Dalmaz, Mahmut Yurt, and Tolga Çukur are with the Department of Electrical and Electronics Engineering, Bilkent University, Ankara, Turkey (e-mails: {onat, mahmut, cukur}@ee.bilkent.edu.tr). T. Çukur is also with the National Magnetic Resonance Research Center, and the Neuroscience Program, Sabuncu Brain Research Center, Bilkent University, TR-06800 Ankara, Turkey.

## Contributions

- We introduce the first adversarial model for medical image synthesis with a transformer-based generator.
- We introduce novel aggregated residual transformer (ART) blocks to synergistically preserve localization and context.
- We introduce a weight sharing strategy among ART blocks to lower model complexity and mitigate computational burden.
- We introduce a unified synthesis model that generalizes across multiple configurations of source-target modalities.

## II. RELATED WORK

The immense success of deep learning in inverse problems has motivated its rapid adoption in medical imaging [50], [51]. Medical image synthesis is a particularly ill-posed problem since target images are predicted without any target-modality data [32]. Earlier studies in this domain have proposed local networks based on patch-level processing [16], [52], [53]. While local networks offer benefits over traditional approaches, they can show limited sensitivity to broader context across images [22]. Later studies adopted deep CNNs for image-level processing with increasing availability of large imaging databases. CNN-based synthesis has been successfully demonstrated in various applications including synthesis across MR scanners [32], [54]–[56], multi-contrast MR synthesis [22], [23], [25]–[28], and CT synthesis [57]–[60]. Despite significant improvements they enable, CNNs trained with pixel-wise loss terms tend to suffer from undesirable loss of detailed structure [24], [43], [44].

To improve capture of structural details, GANs [29] were proposed to learn the distribution of target modalities conditioned on source modalities [61]. Adversarial losses empower GANs to capture an improved prior for recovery of high-spatial-resolution information [24], [43], [44]. In recent years, GAN-based methods were demonstrated to offer state-of-the-art performance in numerous synthesis tasks, including data augmentation as well as multi-modal synthesis [24], [34], [62], [63]. Important applications of GAN models include CT to PET [64], [65], MR to CT [66]–[68], unpaired cross-modality [69]–[72], 3T-to-7T [73], [74], and multi-contrast MRI synthesis [24], [30]–[42].

While GAN models have arguably emerged as a gold standard in recent years, they are not without limitation. In particular, GANs are based on purely convolutional operators known to suffer from poor across-subject generalization to atypical anatomy and sub-optimal learning of long-range spatial dependencies [45], [46]. Recent studies have incorporated spatial or channel attention mechanisms to modulate CNN-derived feature maps [37], [75]–[80]. Such modulation motivates the network to give greater focus to regions that may suffer from greater errors [76], [77]. While attention maps might be distributed across image regions, multiplicative gating of local CNN features offers limited expressiveness in modeling of global context [48], [81].

To explicitly incorporate contextual representations, recent imaging studies have considered transformer-based models for tasks such as segmentation or disease classification [48], [81]–[84]. Closest to our work are few independent efforts in medical image synthesis. [84] used transformers for retinal image

synthesis, [85] included a transformer in the discriminator of a UNet-based GAN for MR-to-PET synthesis, and [86] used a non-adversarial UNet-based performer architecture for one-to-one MRI synthesis in infant brains. Differently from these recent efforts, here we introduce an adversarial transformer architecture inspired by the powerful ResNet model [49]. Novel aggregated residual transformer (ART) blocks are injected in the information bottleneck of ResViT’s generator. Our hybrid CNN-transformer approach consolidates the localization power of convolutional representations with the contextual abilities of transformers. Furthermore, we provide the first demonstrations of a transformer architecture for many-to-one synthesis tasks and a unified synthesis model for advancing practicality over task-specific methods.

## III. THEORY AND METHODS

### A. Residual Vision Transformers

Here we propose a novel adversarial method for medical image synthesis named residual vision transformers, ResViT, that can unify various source-target modality configurations into a single model for improved practicality. ResViT leverages a hybrid architecture of deep convolutional operators and transformer blocks to simultaneously learn high-resolution structural and global contextual features (Fig. 1). It follows an encoder - information bottleneck - decoder pathway in the generator subnetwork, where the bottleneck contains a stack of residual blocks to distill structural and contextual representations. Meanwhile, the discriminator subnetwork is composed of convolutional operators. In the remainder of this section, we explain the detailed composition of each component, and we describe the loss functions to train ResViT.

1) *Encoder*: The first component of ResViT is a deep encoder network that contains a series of convolutional layers to capture a hierarchy of localized features of source images. Note that ResViT can serve a unified synthesis model, so its encoder receives as input the full set of modalities within the imaging protocol, both source and target modalities (Fig. 2). Source modalities are input via an identity mapping, whereas unavailable target modalities are masked out:

$$X_i^G = a_i (\mathbf{1} \cdot m_i) + (1 - a_i) (\mathbf{0} \cdot m_i) \quad (1)$$

where  $i$  denotes the channel index of the encoder input  $i \in \{1, 2, \dots, I\}$ ,  $m_i$  is the image for the  $i$ th modality,  $\mathbf{0}$  is a tensor of zeros, and  $\mathbf{1}$  is a tensor of ones. In Eq. (1),  $a_i$  denotes the availability of the  $i$ th modality:

$$a_i = \begin{cases} 1 & \text{if } m_i \text{ is a source modality} \\ 0 & \text{if } m_i \text{ is a target modality} \end{cases} \quad (2)$$

During training, various different configurations of source-target modalities are considered within the multi-modal protocol (e.g.,  $T_1, T_2 \rightarrow PD$ ;  $T_2, PD \rightarrow T_1$ ;  $T_1, PD \rightarrow T_2$  for a three-contrast MRI protocol). During inference, the specific source-target configuration is determined via the availability conditions in individual test subjects. Given the availability-masked multi-channel input, the encoder uses convolutional operators to learn latent structural representations shared across the consolidated synthesis tasks:

$$encoder(X^G) = f_{n_e} \in \mathbb{R}^{N_C, H, W} \quad (3)$$

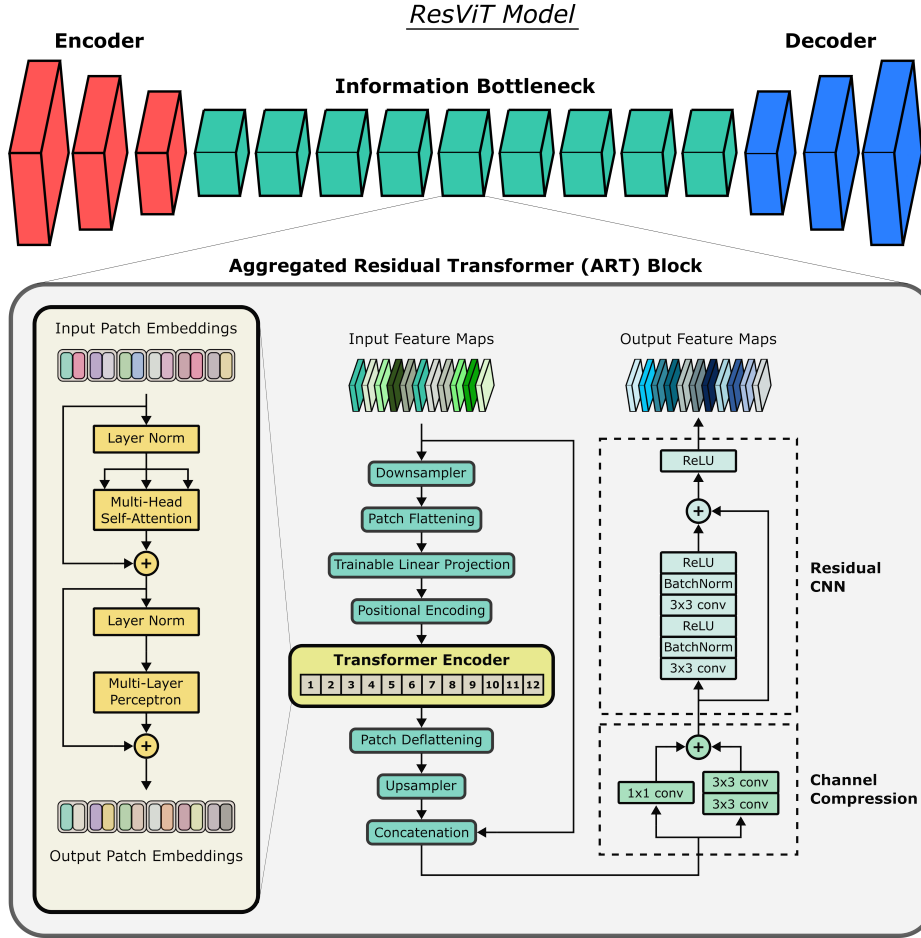


Fig. 1: The generator in ResViT follows an encoder-decoder architecture bridged with a central information bottleneck to distill task-specific information. The encoder and decoder comprise convolutional layers to maintain local precision and inductive bias in learned structural representations. Meanwhile, the information bottleneck comprises a stack of novel aggregated residual transformer (ART) blocks. ART blocks learn contextual representations via vision transformers, and synergistically fuse CNN-based local and transformer-based global representations.

where  $f_{n_e}$  is the embedded latent tensor after  $n_e$  encoder layers,  $N_C$  is the number channels,  $H$  is the height and  $W$  is the width of the tensor. These representations are then fed to the information bottleneck.

**2) Information Bottleneck:** Next, ResViT employs a residual bottleneck to distill task-relevant information in the encoded features. Note that convolution operators have greater power in capturing localized features, whereas attention operators are more sensitive to context-driven features. To simultaneously maintain localization power and contextual sensitivity, we introduce novel aggregated residual transformer (ART) blocks. ART blocks aggregate the information distilled via residual convolutional and transformer branches (Fig. 1). Receiving as input the  $j$ th layer feature maps  $f_j \in \mathbb{R}^{N_C, H, W}$ , an ART block first processes the feature maps via a vision transformer. Due to computational constraints, the transformer expects feature maps at smaller resolutions compared to convolutional layers. Thus, the spatial dimensions ( $H, W$ ) of  $f_j \in \mathbb{R}^{N_C, H, W}$  are lowered by a downsampling block (**DS**):

$$f'_j \in \mathbb{R}^{N'_C, H', W'} = \mathbf{DS}(f_j) \quad (4)$$

where **DS** is implemented as a stack of strided convolutional layers,  $f'_j \in \mathbb{R}^{N'_C, H', W'}$  are downsampled feature maps with  $W' = W/M$ ,  $H' = H/M$ ,  $M$  denoting the downsampling factor. A transformer branch then processes  $f'_j$  to extract contextual information. Accordingly,  $f'_j$  is first split into non-overlapping patches of size  $(P, P)$ , and the patches are then

flattened:

$$\begin{aligned} f_j^1 &= \text{flatten}(f'_j[:, 1:P, 1:P]) \\ f_j^2 &= \text{flatten}(f'_j[:, P+1:2P, 1:P]) \\ &\vdots \\ f_j^{N_P} &= \text{flatten}(f'_j[:, H'-P:H', W'-P:W']) \end{aligned} \quad (5)$$

where  $f_j^p \in \mathbb{R}^{N'_C P^2}$  is the  $p$ th patch where  $p \in \{1, 2, \dots, N_P\}$ , and  $N_P = W'H'/P^2$  are the number of patches. The transformer embeds patches onto an  $N_D$ -dimensional space via trainable linear projections, supplemented with learnable positional encoding:

$$z_0 = [f_j^1 P_E; f_j^2 P_E; \dots; f_j^{N_P} P_E] + P_E^{\text{pos}} \quad (6)$$

where  $z_0 \in \mathbb{R}^{N_P, N_D}$  are the input patch embeddings,  $P_E$  is the embedding projection, and  $P_E^{\text{pos}}$  is the learnable positional encoding.

Next, the transformer encoder processes the patch embeddings via a cascade of  $L$  layers of multi-head self-attention (**MSA**) [87] and multi-layer perceptrons (**MLP**) [88]. The output of the  $l$ th layer in the transformer encoder is expressed as:

$$z'_l = \mathbf{MSA}(\mathbf{LN}(z_{l-1})) + z_{l-1} \quad (7)$$

$$z_l = \mathbf{MLP}(\mathbf{LN}(z'_l)) + z'_l \quad (8)$$

In Eqs. 7-8, **LN** stands for layer normalization [89]:

$$z_l^{\text{LN}} = \mathbf{LN}(z_l) = \frac{z_l - \mu}{\sqrt{\sigma^2 + \epsilon}} \quad (9)$$

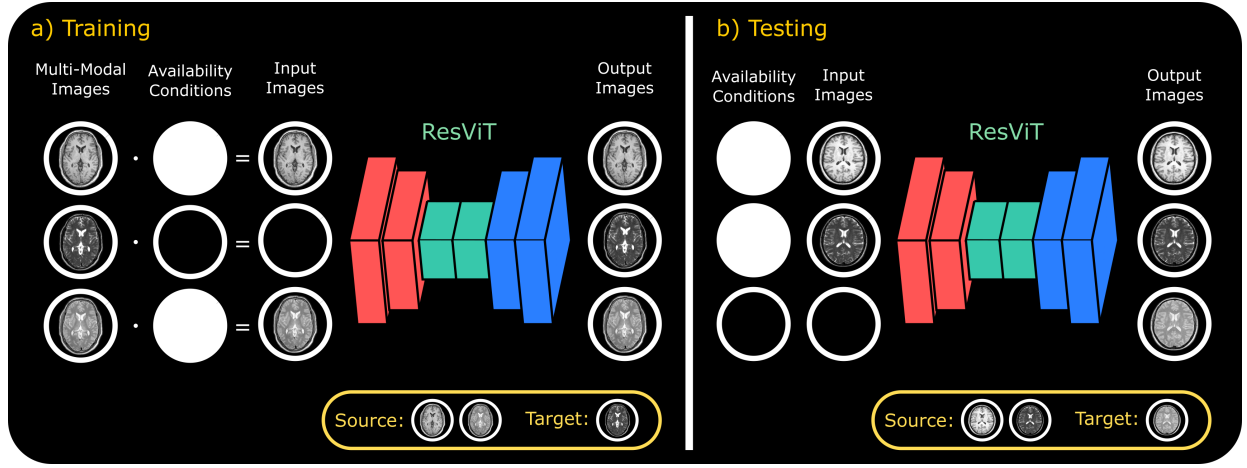


**Fig. 2:** ResViT is a conditional image synthesis model that can unify various source-target modality configurations into a single model for improved practicality. a) During training, ResViT takes as input the entire set of images within the multi-modal protocol, including both source and target modalities. For model consolidation across multiple synthesis tasks, various configurations of source-target modalities are expressed in terms of availability conditions in ResViT. b) During inference, the specific source-target configuration is determined via the availability conditions in each given test subject.

where  $\epsilon$  is a small number preventing division by zero, and  $\mu$ - $\sigma$  are formulated as:

$$\mu = \frac{1}{N_D} \sum_{d=1}^{N_D} z_l(d), \quad \sigma = \sqrt{\frac{1}{N_D} \sum_{d=1}^{N_D} (z_l(d) - \mu)^2} \quad (10)$$

**MSA** layers in Eq. 7 employ  $S$  separate self-attention heads:

$$\mathbf{MSA}(z) = [\mathbf{SA}_1(z); \mathbf{SA}_2(z); \dots; \mathbf{SA}_S(z)] U_{msa} \quad (11)$$

where  $\mathbf{SA}_s$  stands for the  $s$ th attention head with  $s \in \{1, 2, \dots, S\}$  and  $U_{msa}$  denotes the learnable tensor projecting attention head outputs.  $\mathbf{SA}$  layers compute a weighted combination of all elements of the input sequence  $z$ :  $\mathbf{SA}(z) = Av$  where attention weights  $A_{a,b}$  are taken as pairwise similarity between the query  $q$  and key  $k$ :

$$A_{a,b} = \text{softmax}(q_a k_b^T / N_D^{0.5}) \quad (12)$$

The output of the transformer encoder  $z_L$  is then deflattened:

$$g'_j[:, 1:P, 1:P] = \text{deflatten}(z_L[1]) \quad (13)$$

$$g'_j[:, P+1:2P, 1:P] = \text{deflatten}(z_L[2])$$

$\vdots$

$$g'_j[:, H'-P:H', W'-P:W'] = \text{deflatten}(z_L[N_P])$$

where  $g'_j \in \mathbb{R}^{N_D, H', W'}$  is the deflattened feature map. Resolution of  $g'_j$  is increased to match the size of input feature maps via an upsampling block **US** based on transposed convolutions:

$$g_j \in \mathbb{R}^{N_C, H, W} = \mathbf{US}(g'_j) \quad (14)$$

where  $g_j \in \mathbb{R}^{N_C, H, W}$  are upsampled feature maps output by the transformer module. The global context learned via the transformer is then fused with the localized features captured with convolutional operators:

$$h'_j \in \mathbb{R}^{2N_C, H, W} = \text{concat}(f_j, g_j) \quad (15)$$

where  $h'_j$  denotes the concatenated feature maps.

To maintain a fixed tensor size across ART blocks, the channels of the concatenated feature maps are then compressed via a channel compression (**CC**) block:

$$h_j \in \mathbb{R}^{N_C, H, W} = \mathbf{CC}(h'_j) \quad (16)$$

where  $h_j$  are compressed feature maps. **CC** uses two parallel convolutional branches of varying kernel size. Finally, the feature maps are processed via a residual CNN (**ResCNN**) [49] to distill learned structural and contextual representations:

$$f_{j+1} \in \mathbb{R}^{N_C, H, W} = \mathbf{ResCNN}(h_j) \quad (17)$$

where  $f_{j+1}$  denotes the output of the ART block at the  $j$ th network layer.

**3) Decoder:** The last component of the generator is a deep decoder based on transposed convolutional layers. Because ResViT can serve as a unified model, its decoder can synthesize all contrasts within the multi-modal protocol regardless of the specific source-target configuration (Fig. 2). The decoder receives as input the feature maps distilled by the bottleneck and produces multi-modality images in separate channels:

$$\hat{Y}^G = \text{decoder}(f_{n_e+n_i}) \quad (18)$$

where  $f_{n_e+n_i}$  is the output of the bottleneck,  $n_{e,i}$  are numbers of layers in the encoder and bottleneck, and  $\hat{Y}_i^G \in \hat{Y}^G$  denotes the  $i$ th synthesized modality.

**4) Parameter Sharing Transformers:** Multiple ART blocks are used in the information bottleneck to increase the capacity of ResViT in learning contextual representations. That said, multiple independent transformer blocks would inevitably elevate memory demand and risk of overfitting due to an excessive number of parameters. To prevent these risks, a weight-sharing strategy is adopted across ART blocks.

**5) Discriminator:** The discriminator in ResViT is based on a conditional PatchGAN architecture [43]. The discriminator performs patch-level differentiation between acquired and synthetic images. This implementation increases sensitivity to localized details related to high-spatial-frequency information. As ResViT can serve as a unified model by generating all modalities in the multi-modal protocol including sources, an



availability-guided selective discriminator is employed:

$$X_i^D(source) = X_i^G = a_i(\mathbf{1} \cdot m_i) + (1 - a_i)\mathbf{0} \quad (19)$$

$$X_i^D(syn\ target) = (1 - a_i)(\mathbf{1} \cdot Y_i^G) + a_i\mathbf{0} \quad (20)$$

$$X_i^D(acq\ target) = (1 - a_i)(\mathbf{1} \cdot m_i) + a_i\mathbf{0} \quad (21)$$

where  $X_i^D(source)$  are source images,  $X_i^D(syn\ target)$  are synthesized target images, and  $X_i^D(acq\ target)$  are acquired target images. The conditional discriminator receives as input the concatenation of source and target images:

$$X^D(synthetic) = \text{concat}(X_i^D(source), X_i^D(syn\ target)) \quad (22)$$

$$X^D(acquired) = \text{concat}(X_i^D(source), X_i^D(acq\ target)) \quad (23)$$

where  $X^D(synthetic)$  is the concatenation of source and synthetic target images, and  $X^D(acquired)$  is the concatenation of the source and acquired target images.

**6) Loss Function:** The first term in the loss function is a pixel-wise  $L_1$  loss defined between the acquired and synthesized target modalities:

$$L_{pix} = \sum_{i=1}^I (1 - a_i) E[||G(X^G)_i - m_i||_1] \quad (24)$$

where  $E$  denotes expectation, and  $G$  denotes the generator submodule in ResViT. ResViT takes as input source modalities to reconstruct them at the output. Thus, the second term is a pixel-wise consistency loss between acquired and reconstructed source modalities based on an  $L_1$  distance:

$$L_{rec} = \sum_{i=1}^I a_i E[||G(X^G)_i - m_i||_1] \quad (25)$$

The last term is an adversarial loss defined via the conditional discriminator ( $D$ ):

$$L_{adv} = -E[D(X^D(acquired))^2] - E[(D(X^D(synthetic)) - 1)^2] \quad (26)$$

The three terms are linearly combined to form the overall objective:

$$L_{ResViT} = \lambda_{pix} L_{pix} + \lambda_{rec} L_{rec} + \lambda_{adv} L_{adv} \quad (27)$$

where  $\lambda_{pix}$  is the weighting of the pixel-wise loss,  $\lambda_{rec}$  is the weighting of the reconstruction loss, and  $\lambda_{adv}$  is the weighting of the adversarial loss.

## B. Datasets

We demonstrated the proposed ResViT model on two multi-contrast brain MRI datasets (IXI: <https://brain-development.org/ixi-dataset/>, BRATS [90]–[92] and a multi-modal pelvic MRI-CT dataset [93]). Details regarding each dataset are provided in Supp. Text VII-A.

## C. Competing Methods

We demonstrated the proposed ResViT model against several state-of-the-art image synthesis methods. The baseline methods included convolutional models (task-specific models: pGAN [24], pix2pix [43]; unified models: MM-GAN

[41], pGAN<sub>uni</sub>), attention-augmented convolutional models (A-UNet [77], SAGAN [76]), and transformer models (task-specific: TransUNet [48], unified: TransUNet<sub>uni</sub>). Hyperparameters of each competing method were optimized via identical cross-validation procedures. Implementation details of baseline methods are provided in Supp. Text VII-B.

## D. Architectural Details

The architectural parameters of ResViT regarding the generator and discriminator subnetworks are described in detail in Supp. Text VII-C. Since retaining a transformer in each ART block results in significant model complexity, transformer modules utilized tied weights and they were only retained in a subset of ART blocks. The configuration of transformer modules, i.e. their total number and position, was selected via cross-validation experiments as summarized in Supp. Table I (see Supp. Text VII-C for procedures). The complexity of individual transformer modules were also optimized as listed in Supp. Table II. The selected configurations were used in all experiments thereafter.

## E. Modeling Procedures

All models were adversarially trained with the same Patch-GAN discriminator. Task-specific models used adversarial and pixel-wise losses, whereas unified models used adversarial, pixel-wise, and reconstruction losses. For fair comparisons, identical optimization procedures and loss-term weighting were employed for all competing methods. Learning rate schedules, number of epochs, and loss-term weighting were selected via cross-validation. Selected parameters consistently yielded near-optimal performance in all methods. Training was performed via the Adam optimizer [94] with  $\beta_1 = 0.5$ ,  $\beta_2 = 0.999$ . Models were trained for 100 epochs, as further training did not yield any performance improvement. The learning rate was 0.0002 for the first 50 epochs and linearly decayed to 0 in the remaining epochs. Transformer modules in both TransUNet and ResViT were initiated with pre-trained versions for object classification on ImageNet [95]. ART blocks were initiated without transformer modules and then fine-tuned for 50 epochs following insertion of transformers. Loss-term weights were  $\lambda_{adv} = 1$ ,  $\lambda_{pix} = 100$  for task-specific models, and  $\lambda_{adv} = 1$ ,  $\lambda_{rec} = 100$ ,  $\lambda_{pix} = 100$  for unified models. Modelling was performed via the PyTorch framework on nVidia RTX A4000 GPUs. Inference times are listed in Supp. Table III. Code to replicate the ResViT model is publicly available at <https://github.com/icon-lab>.

Synthesis quality was assessed via Peak Signal to Noise Ratio (PSNR), and Structural Similarity Index (SSIM) [96]. Metrics were calculated between ground truth and synthesized target images. Mean and standard deviations of metrics were reported across an independent test set, non-overlapping with training-validation sets. Significance of performance differences were evaluated with signed-rank tests ( $p < 0.05$ ). Tests were conducted on subject-average metrics, except MRI  $\rightarrow$  CT where cross-sectional metrics were tested in each subject due to limited number of test subjects.

## F. Experiments

**1) Multi-Contrast MRI Synthesis:** Experiments were conducted on the IXI and BRATS datasets to demonstrate synthesis performance in multi-modal MRI. In the IXI dataset, one-to-one tasks of  $T_2 \rightarrow PD$ ;  $PD \rightarrow T_2$  and many-to-one tasks

	$T_1, T_2 \rightarrow PD$		$T_1, PD \rightarrow T_2$		$T_2, PD \rightarrow T_1$	
	PSNR	SSIM	PSNR	SSIM	PSNR	SSIM
ResViT	<b>33.92</b> $\pm 1.44$	<b>0.977</b> $\pm 0.004$	<b>35.71</b> $\pm 1.20$	<b>0.977</b> $\pm 0.005$	<b>29.58</b> $\pm 1.37$	<b>0.952</b> $\pm 0.011$
pGAN	32.91 $\pm 0.94$	0.966 $\pm 0.005$	33.95 $\pm 1.06$	0.965 $\pm 0.006$	28.71 $\pm 1.08$	0.941 $\pm 0.013$
pix2pix	32.25 $\pm 1.24$	0.974 $\pm 0.006$	33.62 $\pm 1.31$	0.973 $\pm 0.009$	28.35 $\pm 1.24$	0.949 $\pm 0.016$
A-UNet	32.24 $\pm 0.92$	0.963 $\pm 0.014$	32.43 $\pm 1.36$	0.959 $\pm 0.007$	28.95 $\pm 1.21$	0.916 $\pm 0.013$
SAGAN	32.50 $\pm 0.93$	0.964 $\pm 0.005$	33.71 $\pm 1.00$	0.965 $\pm 0.006$	28.62 $\pm 1.10$	0.942 $\pm 0.013$
TransUNet	32.53 $\pm 0.97$	0.968 $\pm 0.005$	32.49 $\pm 1.18$	0.960 $\pm 0.008$	28.21 $\pm 1.30$	0.941 $\pm 0.013$

**TABLE I:** Performance of task-specific synthesis models in many-to-one tasks ( $T_1, T_2 \rightarrow PD$ ,  $T_1, PD \rightarrow T_2$ , and  $T_2, PD \rightarrow T_1$ ) in the IXI dataset. PSNR (dB) and SSIM (%) are listed as mean $\pm$ std across test subjects. Boldface indicates the top-performing model for each task.

of  $T_1, T_2 \rightarrow PD$ ;  $T_1, PD \rightarrow T_2$ ;  $T_2, PD \rightarrow T_1$  were considered. In the BRATS dataset, one-to-one tasks of  $T_2 \rightarrow FLAIR$ ;  $FLAIR \rightarrow T_2$ , many-to-one tasks of  $T_1, T_2 \rightarrow FLAIR$ ;  $T_1, FLAIR \rightarrow T_2$ ;  $T_2, FLAIR \rightarrow T_1$  were considered. In both datasets, task-specific ResViT models were compared against pGAN, pix2pix, A-UNet, SAGAN, and TransUNet. Meanwhile, unified ResViT models were demonstrated against pGAN<sub>uni</sub>, MM-GAN, and TransUNet<sub>uni</sub>.

2) *MRI to CT Synthesis:* Experiments were performed on the MRI-CT dataset to demonstrate across-modality synthesis performance. A one-to-one synthesis task of deriving target CT images from source MR images was considered. The task-specific ResViT model was compared against pGAN, pix2pix, A-UNet, SAGAN, and TransUNet.

3) *Ablation Studies:* Several lines of ablation experiments were conducted to demonstrate the value of the individual components of the ResViT model. These components included transformer modules, convolutional modules, adversarial learning, configuration of ART blocks, and training strategies. Self-attention maps in transformer modules were also derived for visual interpretation. Experiments were performed on three representative tasks: namely  $T_1, T_2 \rightarrow PD$  in IXI,  $T_1, T_2 \rightarrow FLAIR$  in BRATS, and  $MRI \rightarrow CT$ . Detailed procedures are provided in Supp. Text VII-D.

## IV. RESULTS

### A. Multi-Contrast MRI Synthesis

1) *Task-Specific Synthesis Models:* We demonstrated the performance of ResViT in learning task-specific synthesis models for multi-contrast MRI. ResViT was compared against convolutional models (pGAN, pix2pix), attention-augmented CNNs (A-UNet, SAGAN), and a recent transformer architecture (TransUNet). First, brain images of healthy subjects in the IXI dataset were considered. PSNR and SSIM metrics are listed in Table I for many-to-one and Supp. Table IV for one-to-one tasks. ResViT achieves the highest performance in both many-to-one ( $p < 0.05$ ) and one-to-one tasks ( $p < 0.05$ ). On average, ResViT outperforms convolutional models by 1.62 dB PSNR and 0.85% SSIM, attention-augmented models by 1.40 dB PSNR and 1.45% SSIM, and TransUNet by 2.10 dB PSNR and 1.26% SSIM ( $p < 0.05$ ). Representative images for  $T_1, T_2 \rightarrow PD$  and  $T_2, PD \rightarrow T_1$  are displayed in Supp. Fig. 1

	$T_1, T_2 \rightarrow FLAIR$		$T_1, FLAIR \rightarrow T_2$		$T_2, FLAIR \rightarrow T_1$	
	PSNR	SSIM	PSNR	SSIM	PSNR	SSIM
ResViT	<b>25.84</b> $\pm 1.13$	<b>0.886</b> $\pm 0.014$	<b>26.90</b> $\pm 1.20$	<b>0.938</b> $\pm 0.011$	<b>26.20</b> $\pm 1.31$	<b>0.924</b> $\pm 0.009$
pGAN	24.89 $\pm 1.10$	0.867 $\pm 0.015$	26.51 $\pm 1.13$	0.922 $\pm 0.012$	25.72 $\pm 1.54$	0.918 $\pm 0.011$
pix2pix	24.31 $\pm 1.21$	0.862 $\pm 0.015$	26.12 $\pm 1.53$	0.920 $\pm 0.012$	25.80 $\pm 1.72$	0.918 $\pm 0.011$
A-UNet	24.36 $\pm 1.24$	0.857 $\pm 0.017$	26.48 $\pm 1.21$	0.924 $\pm 0.012$	25.67 $\pm 1.35$	0.918 $\pm 0.010$
SAGAN	24.62 $\pm 1.17$	0.869 $\pm 0.014$	26.41 $\pm 1.22$	0.919 $\pm 0.012$	25.91 $\pm 1.42$	0.918 $\pm 0.011$
TransUNet	24.34 $\pm 1.26$	0.872 $\pm 0.014$	26.51 $\pm 0.92$	0.920 $\pm 0.010$	25.76 $\pm 1.69$	0.921 $\pm 0.011$

**TABLE II:** Performance of task-specific synthesis models in many-to-one tasks ( $T_1, T_2 \rightarrow FLAIR$ ,  $T_1, FLAIR \rightarrow T_2$ , and  $T_2, FLAIR \rightarrow T_1$ ) across test subjects in the BRATS dataset. Boldface indicates the top-performing model for each task.

a,b. Compared to baselines, ResViT synthesizes target images with lower artifact levels and sharper tissue depiction.

We then demonstrated task-specific ResViT models on the BRATS dataset containing images of glioma patients. PSNR and SSIM metrics are listed in Table II for many-to-one and Supp. Table V for one-to-one tasks. ResViT again achieves the highest performance in many-to-one ( $p < 0.05$ ) and one-to-one tasks ( $p < 0.05$ ), except  $T_2 \rightarrow FLAIR$  where A-UNet has slightly higher SSIM. On average, ResViT outperforms convolutional models by 0.92 dB PSNR and 1.29% SSIM, attention-augmented models by 0.84 dB PSNR and 1.24% SSIM, and TransUNet by 0.94 dB PSNR and 1.10% SSIM ( $p < 0.05$ ). Note that the BRATS dataset contains pathology with large across-subject variability. As expected, attention-augmented models show relative benefits against pure convolutional models, yet ResViT that explicitly models contextual relationships still outperforms all baselines. Representative target images for  $T_1, T_2 \rightarrow FLAIR$  and  $T_2, FLAIR \rightarrow T_1$  are displayed in Fig. 3 a,b, respectively. Compared to baselines, ResViT synthesizes target images with lower artifact levels and sharper tissue depiction. Importantly, ResViT reliably captures brain lesions in patients in contrast to competing methods with inaccurate depictions including TransUNet (see Supp. Text VII-E for discussion of contributing factors to performance differences between ResViT and TransUNet).

2) *Unified Synthesis Models:* Task-specific models are trained and tested to perform a single synthesis task to improve performance, but a separate model has to be built for each task. Next, we demonstrated ResViT in learning unified synthesis models for multi-contrast MRI. A unified ResViT (ResViT<sub>uni</sub>) was compared against unified convolutional (pGAN<sub>uni</sub>, MM-GAN) and transformer models (TransUNet<sub>uni</sub>). Performance of unified models were evaluated at test time on many-to-one tasks in IXI (Table III) and BRATS (Table IV). ResViT<sub>uni</sub> maintains the highest performance in many-to-one tasks in both IXI ( $p < 0.05$ ) and BRATS ( $p < 0.05$ ). In IXI, ResViT<sub>uni</sub> outperforms pGAN<sub>uni</sub> by 1.12 dB PSNR and 0.70% SSIM, MM-GAN by 2.37 dB PSNR and 1.80% SSIM, and TransUNet<sub>uni</sub> by 2.69 dB PSNR and 1.67% SSIM ( $p < 0.05$ ). In BRATS, ResViT outperforms pGAN<sub>uni</sub> by 0.74 dB PSNR and 0.93% SSIM, MM-GAN by 0.77 dB PSNR and 0.90% SSIM, and TransUNet<sub>uni</sub> by 1.08 dB PSNR and 1.43% SSIM ( $p < 0.05$ ). Representative target images are displayed in Supp. Fig. 2. ResViT synthesizes target images with lower

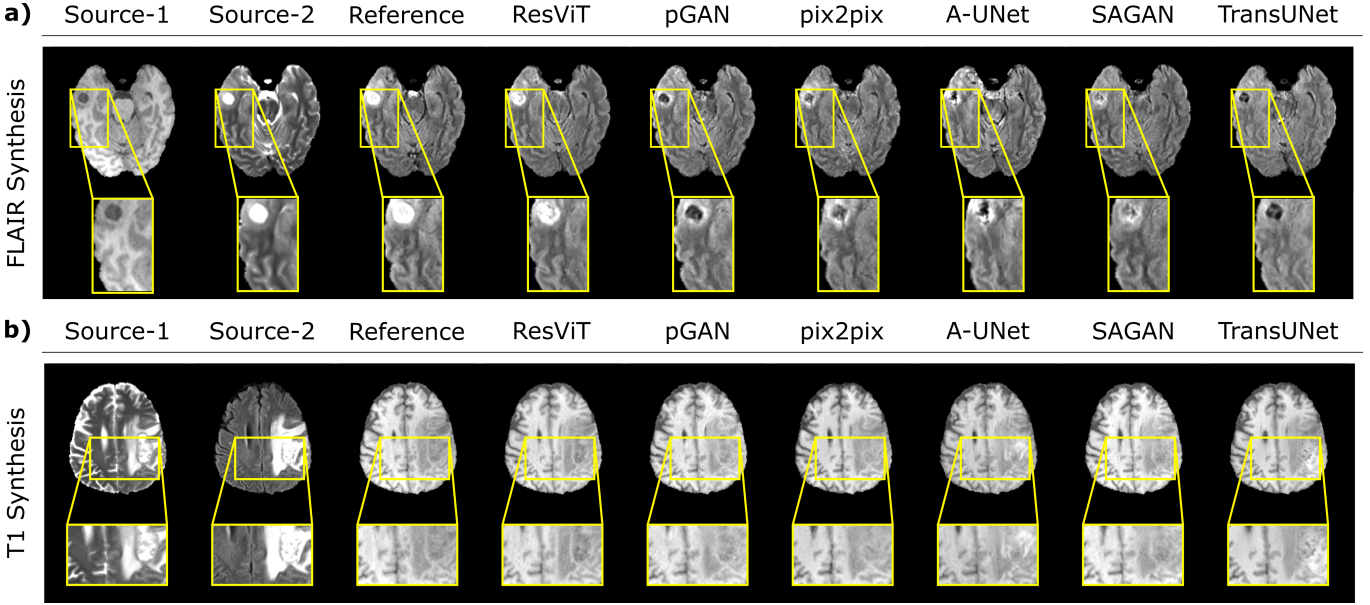


**Fig. 3:** ResViT was demonstrated on the BRATS dataset for two representative many-to-one synthesis tasks: a)  $T_1, T_2 \rightarrow \text{FLAIR}$ , b)  $T_2, \text{FLAIR} \rightarrow T_1$ . Synthesized images from all competing methods are shown along with the source images and the reference image. ResViT improves synthesis performance, especially in pathological regions (e.g., tumors, lesions) in comparison to competing methods. Overall, ResViT images have better-delineated tissue boundaries and lower artifact/noise levels.

	$T_1, T_2 \rightarrow \text{PD}$		$T_1, \text{PD} \rightarrow T_2$		$T_2, \text{PD} \rightarrow T_1$	
	PSNR	SSIM	PSNR	SSIM	PSNR	SSIM
ResViT <sub>uni</sub>	<b>33.22</b>	<b>0.971</b>	<b>33.97</b>	<b>0.968</b>	<b>28.80</b>	<b>0.946</b>
	$\pm 1.21$	$\pm 0.005$	$\pm 1.04$	$\pm 0.006$	$\pm 1.20$	$\pm 0.013$
pGAN <sub>uni</sub>	31.86	0.965	32.90	0.962	27.86	0.937
	$\pm 1.09$	$\pm 0.005$	$\pm 0.91$	$\pm 0.006$	$\pm 1.04$	$\pm 0.014$
MM-GAN	30.73	0.955	30.91	0.951	27.23	0.925
	$\pm 1.16$	$\pm 0.006$	$\pm 1.61$	$\pm 0.013$	$\pm 1.24$	$\pm 0.015$
TransUNet <sub>uni</sub>	30.30	0.956	30.77	0.949	26.86	0.930
	$\pm 1.44$	$\pm 0.007$	$\pm 1.10$	$\pm 0.014$	$\pm 1.16$	$\pm 0.013$

**TABLE III:** Performance of unified synthesis models in many-to-one tasks  $T_1, T_2 \rightarrow \text{PD}$ ,  $T_1, \text{PD} \rightarrow T_2$ , and  $T_2, \text{PD} \rightarrow T_1$ ) across test subjects in the IXI dataset. Boldface indicates the top-performing model for each task.

	$T_1, T_2 \rightarrow \text{FLAIR}$		$T_1, \text{FLAIR} \rightarrow T_2$		$T_2, \text{FLAIR} \rightarrow T_1$	
	PSNR	SSIM	PSNR	SSIM	PSNR	SSIM
ResViT <sub>uni</sub>	<b>25.32</b>	<b>0.876</b>	<b>26.81</b>	<b>0.921</b>	<b>26.24</b>	<b>0.922</b>
	$\pm 0.91$	$\pm 0.015$	$\pm 1.04$	$\pm 0.012$	$\pm 1.65$	$\pm 0.010$
pGAN <sub>uni</sub>	24.46	0.865	26.23	0.914	25.46	0.912
	$\pm 0.99$	$\pm 0.014$	$\pm 1.08$	$\pm 0.012$	$\pm 1.20$	$\pm 0.009$
MM-GAN	24.20	0.861	26.10	0.915	25.75	0.916
	$\pm 1.34$	$\pm 0.015$	$\pm 1.48$	$\pm 0.014$	$\pm 1.64$	$\pm 0.011$
TransUNet <sub>uni</sub>	24.11	0.863	26.05	0.912	24.96	0.901
	$\pm 1.19$	$\pm 0.014$	$\pm 1.46$	$\pm 0.013$	$\pm 1.24$	$\pm 0.012$

**TABLE IV:** Performance of unified synthesis models in many-to-one tasks ( $T_1, T_2 \rightarrow \text{FLAIR}$ ,  $T_1, \text{FLAIR} \rightarrow T_2$ , and  $T_2, \text{FLAIR} \rightarrow T_1$ ) across test subjects in the BRATS dataset. Boldface indicates the top-performing model for each task.

artifacts and sharper depiction than baselines. These results suggest that a unified ResViT model can successfully consolidate models for varying source-target configurations.

### B. Across-Modality Synthesis

We also demonstrated ResViT in across-modality synthesis.  $T_2$ -weighted MRI and CT images in the pelvic dataset were considered. ResViT was compared against pGAN, pix2pix, A-UNet, SAGAN, and TransUNet. PSNR and SSIM metrics are listed in Table V. ResViT yields the highest performance in each subject ( $p < 0.05$ ). On average, ResViT outperforms

		ResViT	pGAN	pix2pix	A-UNet	SAGAN	TransUNet
	PSNR	<b>28.45</b>	26.80	26.53	27.80	27.61	27.76
		$\pm 1.35$	$\pm 0.90$	$\pm 0.45$	$\pm 0.63$	$\pm 1.02$	$\pm 1.03$
	SSIM	<b>0.931</b>	0.905	0.898	0.913	0.910	0.914
MRI $\rightarrow$ CT	SSIM	$\pm 0.009$	$\pm 0.008$	$\pm 0.004$	$\pm 0.004$	$\pm 0.006$	$\pm 0.009$

**TABLE V:** Performance for the across-modality synthesis task ( $T_2$ -weighted MRI  $\rightarrow$  CT) across test subjects in the pelvic MRI-CT dataset. Boldface indicates the top-performing model for each task.

convolutional models by 1.79 dB PSNR and 2.95% SSIM, attention-augmented models by 0.75 dB PSNR and 1.95% SSIM, and TransUNet by 0.69 dB PSNR and 1.7% SSIM ( $p < 0.05$ ). Representative target images are displayed in Fig. 4. Compared to baselines, ResViT synthesizes target images with lower artifacts and more accurate tissue depiction. Differently from multi-contrast MRI, attention-augmented models and TransUNet offer more noticeable performance benefits over convolutional models. That said, ResViT still maintains further elevated performance, particularly near bone structures in CT images. This finding suggests that the relative importance of contextual representations is higher in MRI-CT synthesis. With the help of its residual transformer blocks, ResViT offers reliable performance with accurate tissue depiction in this task.

### C. Ablation Studies

We performed a systematic set of experiments to demonstrate the added value of the main components and training strategies used in ResViT. First, we compared ResViT against ablated variants where the convolutional modules in ART blocks, transformer modules in ART blocks, or the adversarial term in training loss were separately removed. Supp. Table VI lists performance metrics in the test set for three representative synthesis tasks. Consistently across tasks, ResViT yields optimal or near-optimal performance. ResViT achieves higher PSNR and SSIM in representative tasks compared to variants without transformer or convolutional modules ( $p < 0.05$ ). It



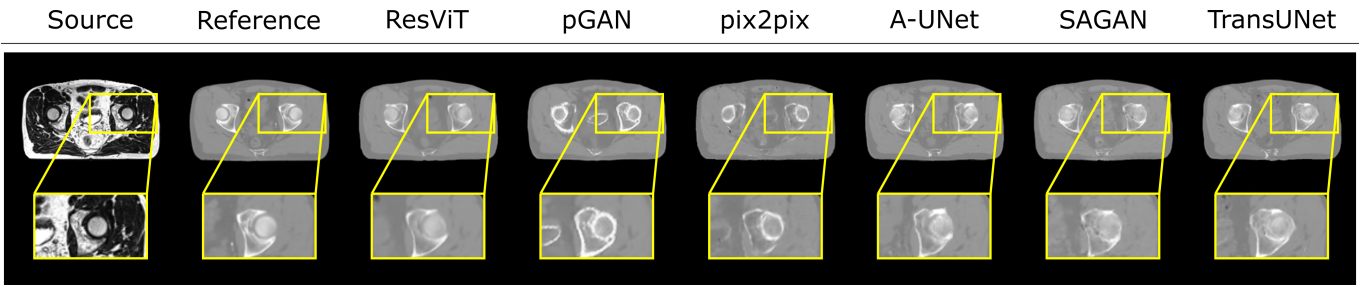


Fig. 4: ResViT was demonstrated on the pelvic MRI-CT dataset for the  $T_2$ -weighted MRI  $\rightarrow$  CT task. Synthesized images from all competing methods are shown along with the source and reference images. ResViT enhances synthesis of relevant morphology in the CT domain as evidenced by the elevated accuracy near bone structures.

also yields lower FID than these variants, except in MRI  $\rightarrow$  CT where ablation of the convolutional module slightly decreases FID. Importantly, ResViT maintains notably lower FID compared to the variant without adversarial loss (albeit slightly lower SSIM in  $T_1$ ,  $T_2 \rightarrow$  FLAIR and PSNR in MRI  $\rightarrow$  CT). This is expected since FID is generally considered as a more suited metric to examine the perceptual benefits of adversarial learning than PSNR or SSIM that reflect heavier influence from relatively lower frequencies [97]. Representative synthesized images are also displayed in Supp. Fig. 3. ResViT images more closely mimic the reference images, and show greater spatial acuity compared against the variant without adversarial loss. Taken together, these results indicate that adversarial learning enables ResViT to more closely capture the distributional properties of target-modality images.

Next, we compared ResViT against ablated variants where the weight tying procedure across transformer modules was neglected, or transformer modules in one of the two retaining ART blocks were removed. Supp. Table VII lists performance metrics in the test set. ResViT yields higher performance than all variants in representative tasks ( $p < 0.05$ ). These results demonstrate the added value of the weight tying procedure and the transformer configuration in ResViT. We also compared ResViT against ablated variants where the pre-training of transformer modules or their delayed insertion during training were selectively neglected, as listed in Supp. Table VIII. Our results indicate that both pre-training and delayed insertion of transformers improve synthesis performance in representative tasks ( $p < 0.05$ ).

Lastly, we wanted to visually interpret the benefits of the self-attention mechanisms in ResViT towards synthesis performance. Supp. Fig. 4 displays representative attention maps in ResViT. Synthetic images and error maps are also shown for ResViT as well as pGAN, which generally offered the closest performance to ResViT in our experiments. There is a high degree of correlation among the regions where the attention maps focus on and the image regions where ResViT yields substantially reduced error levels compared to pGAN. These visual observations imply that the self-attention mechanisms in ResViT strengthen contextual representations to yield lower synthesis errors.

## V. DISCUSSION

In this study, we proposed a novel adversarial model for image translation between separate modalities. Traditional GANs employ convolutional operators that have limited ability to capture long-range relationships among distant regions [46]. The proposed model aggregates convolutional and transformer

branches within a residual bottleneck to preserve both local precision and contextual sensitivity. To our knowledge, this is the first adversarial model for medical image synthesis with a transformer-based generator. We further introduced a weight-sharing strategy among transformer modules to lower model complexity. Finally, a unification strategy was implemented to learn an aggregate model that copes with numerous source-target configurations without training separate models.

We demonstrated ResViT for missing sequence synthesis tasks in multi-contrast MRI and missing modality synthesis in multi-modal MRI-CT imaging. Comparisons were provided against state-of-the-art convolutional models with UNet and ResNet backbones and a recent transformer architecture with UNet backbone. ResViT outperforms competing methods in one-to-one and many-to-one synthesis tasks, and our results demonstrate the efficiency of ResViT in maintaining contextual and local representations.

Trained with image-average loss terms, CNNs have difficulty in coping with atypical anatomy that substantially varies across subjects [24], [43]. To improve generalization, recent studies have proposed self-attention mechanisms in GAN models over spatial or channel dimensions [76], [77]. Specifically, attention maps are used for multiplicative modulation of CNN-derived feature maps. This modulation encourages the network to focus on critical image regions with relatively limited task performance. While attention maps can be distributed across image regions, they mainly capture implicit contextual information via modification of local CNN features. Since feature representations are primarily extracted via convolutional filtering, the resulting model can still manifest limited expressiveness for global context. In contrast, the proposed architecture uses dedicated transformer blocks to explicitly model long-range spatial interactions in medical images.

Few recent studies have independently proposed transformer-based models for medical image synthesis tasks [84]–[86]. In [85], a transformer was included in the discriminator of a traditional GAN for MRI-to-PET synthesis. In [86], a UNet-inspired transformer architecture was proposed for infant MRI synthesis [86]. Differing from these efforts, our work makes the following contributions. (1) Compared to [85] that uses transformers to learn a prior for target PET images, we employ transformers in ResViT’s generator to learn latent contextual representations of source images. (2) Unlike [86] that uses mean-squared error loss amenable to over-smoothing of target images [24], we leverage an adversarial loss to preserve realism. (3) [86] uses transformers across all segments of a UNet-based architecture. We instead propose a ResNet-inspired hybrid



architecture that combines localization capabilities of CNNs with contextual sensitivity of transformers. (4) While [85] and [86] consider only task-specific, one-to-one synthesis models, here we uniquely introduce many-to-one synthesis models and a unified model that generalizes across multiple source-target configurations.

Several lines of development can help further improve ResViT's performance. Here, we considered synthesis tasks in which source and target modalities were registered prior to training, and they were paired across subjects. When registration accuracy is limited, a spatial registration block can be incorporated into the network. Furthermore, a cycle-consistency loss [44] can be incorporated in the optimization objective to allow the use of unregistered images. This latter strategy would also permit training of ResViT models on unpaired datasets [67], [68]. Finally, data requirements for model training can be further alleviated by adopting semi-supervised strategies that allow mixing of paired and unpaired training data [66], or that would enable training of synthesis models directly from undersampled acquisitions [98].

## VI. CONCLUSION

Here we introduced a novel synthesis approach for multi-modal imaging based on a conditional deep adversarial network. In an information bottleneck, ResViT aggregates convolutional operators and vision transformers, thereby improving capture of contextual relations while maintaining localization power. A unified implementation was introduced that prevents the need to rebuild models for varying source-target configurations. ResViT achieves superior synthesis quality to state-of-the-art approaches in multi-contrast brain MRI and multi-modal pelvic MRI-CT datasets. Therefore, it holds promise as a powerful candidate for medical image synthesis.

## REFERENCES

- [1] B. J. Pichler, M. S. Judenhofer, and C. Pfannenberger, *Multimodal Imaging Approaches: PET/CT and PET/MRI*. Springer, 2008, pp. 109–132.
- [2] B. Moraal, S. Roosaendaal, P. Pouwels, H. Vrenken, R. Schijndel, D. Meier, C. Guttman, J. Geurts *et al.*, “Multi-contrast, isotropic, single-slab 3d MR imaging in multiple sclerosis,” *European radiology*, vol. 18, pp. 2311–2320, 2008.
- [3] B. Thukral, “Problems and preferences in pediatric imaging,” *Indian Journal of Radiology and Imaging*, vol. 25, pp. 359–364, 2015.
- [4] K. Krupa and M. Bekiesińska-Figatowska, “Artifacts in magnetic resonance imaging,” *Polish Journal of Radiology*, vol. 80, pp. 93–106, 2015.
- [5] J. E. Iglesias, E. Konukoglu, D. Zikic, B. Glocker, K. Van Leemput, and B. Fischl, “Is synthesizing MRI contrast useful for inter-modality analysis?” in *MICCAI*. Springer, 2013, pp. 631–638.
- [6] Y. Huo, Z. Xu, S. Bao, A. Assad, R. G. Abramson, and B. A. Landman, “Adversarial synthesis learning enables segmentation without target modality ground truth,” in *Proceedings of IEEE ISBI*, 2018, pp. 1217–1220.
- [7] S. Farsiu, D. Robinson, M. Elad, and P. Milanfar, “Advances and challenges in super-resolution,” *International Journal of Imaging Systems and Technology*, vol. 14, pp. 47–57, 2004.
- [8] D. H. Ye, D. Zikic, B. Glocker, A. Criminisi, and E. Konukoglu, “Modality propagation: Coherent synthesis of subject-specific scans with data-driven regularization,” in *MICCAI*. Springer, 2013, pp. 606–613.
- [9] C. Catana, A. van der Kouwe, T. Benner, C. J. Michel, M. Hamm, M. Fenchel, B. Fischl, B. Rosen *et al.*, “Toward implementing an MRI-based PET attenuation-correction method for neurologic studies on the MR-PET brain prototype,” *Journal of Nuclear Medicine*, vol. 51, no. 9, pp. 1431–1438, 2010.
- [10] J. Lee, A. Carass, A. Jog, C. Zhao, and J. Prince, “Multi-atlas-based CT synthesis from conventional MRI with patch-based refinement for MRI-based radiotherapy planning,” in *Proceedings of SPIE*, vol. 10133, 2017, p. 101331I.
- [11] S. Roy, A. Jog, A. Carass, and J. L. Prince, “Atlas based intensity transformation of brain MR images,” in *Multimodal Brain Image Analysis*. Springer, 2013, pp. 51–62.
- [12] Y. Huang, L. Shao, and A. F. Frangi, “Simultaneous super-resolution and cross-modality synthesis of 3d medical images using weakly-supervised joint convolutional sparse coding,” *Proceedings of CVPR*, pp. 5787–5796, 2017.
- [13] —, “Cross-modality image synthesis via weakly coupled and geometry co-regularized joint dictionary learning,” *IEEE Transactions on Medical Imaging*, vol. 37, no. 3, pp. 815–827, 2018.
- [14] C. Zhao, A. Carass, J. Lee, Y. He, and J. L. Prince, “Whole brain segmentation and labeling from CT using synthetic MR images,” in *Machine Learning in Medical Imaging*. Springer, 2017, pp. 291–298.
- [15] A. Jog, A. Carass, S. Roy, D. L. Pham, and J. L. Prince, “Random forest regression for magnetic resonance image synthesis,” *Medical Image Analysis*, vol. 35, pp. 475–488, 2017.
- [16] H. Van Nguyen, K. Zhou, and R. Vemulapalli, “Cross-domain synthesis of medical images using efficient location-sensitive deep network,” in *MICCAI*. Springer, 2015, pp. 677–684.
- [17] R. Vemulapalli, H. Van Nguyen, and S. K. Zhou, “Unsupervised cross-modal synthesis of subject-specific scans,” in *Proceedings of ICCV*, 2015, pp. 630–638.
- [18] Y. Wu, W. Yang, L. Lu, Z. Lu, L. Zhong, M. Huang, Y. Feng, Q. Feng *et al.*, “Prediction of CT substitutes from MR images based on local diffeomorphic mapping for brain PET attenuation correction,” *Journal of Nuclear Medicine*, vol. 57, no. 10, pp. 1635–1641, 2016.
- [19] D. C. Alexander, D. Zikic, J. Zhang, H. Zhang, and A. Criminisi, “Image quality transfer via random forest regression: Applications in diffusion MRI,” in *MICCAI*. Springer, 2014, pp. 225–232.
- [20] T. Huynh, Y. Gao, J. Kang, L. Wang, P. Zhang, J. Lian, and D. Shen, “Estimating CT image from MRI data using structured random forest and auto-context model,” *IEEE Transactions on Medical Imaging*, vol. 35, no. 1, pp. 174–183, 2016.
- [21] P. Coupe, J. V. Manjón, M. Chamberland, M. Descoteaux, and B. Hiba, “Collaborative patch-based super-resolution for diffusion-weighted images,” *NeuroImage*, vol. 83, pp. 245–261, 2013.
- [22] V. Sevetlidis, M. V. Giuffrida, and S. A. Tsaftaris, “Whole image synthesis using a deep encoder-decoder network,” in *Simulation and Synthesis in Medical Imaging*. Springer, 2016, pp. 127–137.
- [23] A. Chatsias, T. Joyce, M. V. Giuffrida, and S. A. Tsaftaris, “Multimodal MR synthesis via modality-invariant latent representation,” *IEEE Transactions on Medical Imaging*, vol. 37, no. 3, pp. 803–814, 2018.
- [24] S. U. Dar, M. Yurt, L. Karacan, A. Erdem, E. Erdem, and T. Çukur, “Image synthesis in multi-contrast MRI with conditional generative adversarial networks,” *IEEE Transactions on Medical Imaging*, vol. 38, no. 10, pp. 2375–2388, 2019.
- [25] C. Bowles, C. Qin, C. Ledig, R. Guerrero, R. Gunn, A. Hammers, E. Sakka, D. Dickie *et al.*, “Pseudo-healthy image synthesis for white matter lesion segmentation,” in *Simulation and Synthesis in Medical Imaging*. Springer, 2016, pp. 87–96.
- [26] N. Cordier, H. Delingette, M. Le, and N. Ayache, “Extended modality propagation: Image synthesis of pathological cases,” *IEEE Transactions on Medical Imaging*, vol. 35, pp. 2598–2608, 2016.
- [27] T. Joyce, A. Chatsias, and S. A. Tsaftaris, “Robust multi-modal MR image synthesis,” in *MICCAI*. Springer, 2017, pp. 347–355.
- [28] W. Wei, E. Poirion, B. Bodini, S. Durrleman, O. Colliot, B. Stankoff, and N. Ayache, “Fluid-attenuated inversion recovery MRI synthesis from multisequence MRI using three-dimensional fully convolutional networks for multiple sclerosis,” *Journal of Medical Imaging*, vol. 6, no. 1, p. 014005, 2019.
- [29] I. Goodfellow, J. Pouget-Abadie, M. Mirza, B. Xu, D. Warde-Farley, S. Ozair, A. Courville, and Y. Bengio, “Generative adversarial networks,” *Proceedings of NIPS*, vol. 24, 2014.
- [30] A. Beers, J. Brown, K. Chang, J. Campbell, S. Ostmo, M. Chiang, and J. Kalpathy-Cramer, “High-resolution medical image synthesis using progressively grown generative adversarial networks,” *arXiv:1805.03144*, 2018.
- [31] B. Yu, L. Zhou, L. Wang, J. Fripp, and P. Bourgeat, “3d cGAN based cross-modality MR image synthesis for brain tumor segmentation,” *Proceedings of IEEE ISBI*, pp. 626–630, 2018.
- [32] D. Nie, R. Trullo, J. Lian, L. Wang, C. Petitjean, S. Ruan, and Q. Wang, “Medical image synthesis with deep convolutional adversarial networks,” *IEEE Transactions on Biomedical Engineering*, vol. 65, no. 12, pp. 2720–2730, 2018.
- [33] K. Armanious, C. Jiang, M. Fischer, T. Küstner, T. Hepp, K. Nikolaou, S. Gatidis, and B. Yang, “MedGAN: Medical image translation using GANs,” *Computerized Medical Imaging and Graphics*, vol. 79, p. 101684, 2019.
- [34] D. Lee, J. Kim, W.-J. Moon, and J. C. Ye, “CollaGAN: Collaborative GAN for missing image data imputation,” in *Proceedings of CVPR*, 2019, pp. 2487–2496.
- [35] H. Li, J. C. Paetzold, A. Sekuboyina, F. Kofler, J. Zhang, J. S. Kirschke, B. Wiestler, and B. Menze, “Diamondgan: Unified multi-modal generative adversarial networks for MRI sequences synthesis,” in *MICCAI*. Springer, 2019, pp. 795–803.
- [36] T. Zhou, H. Fu, G. Chen, J. Shen, and L. Shao, “Hi-net: Hybrid-fusion network for multi-modal MR image synthesis,” *IEEE Transactions on Medical Imaging*, vol. 39, no. 9, pp. 2772–2781, 2020.

- [37] H. Lan, A. Toga, and F. Sepehrband, "Sc-GAN: 3d self-attention conditional GAN with spectral normalization for multi-modal neuroimaging synthesis," *bioRxiv:2020.06.09.143297*, 2020.
- [38] M. Yurt, S. U. Dar, A. Erdem, E. Erdem, K. K. Oguz, and T. Çukur, "mustGAN: multi-stream generative adversarial networks for MR image synthesis," *Medical Image Analysis*, vol. 70, p. 101944, 2021.
- [39] H. Yang, X. Lu, S.-H. Wang, Z. Lu, J. Yao, Y. Jiang, and P. Qian, "Synthesizing multi-contrast MR images via novel 3d conditional variational auto-encoding GAN," *Mobile Networks and Applications*, vol. 26, pp. 1–10, 2021.
- [40] B. Yu, L. Zhou, L. Wang, Y. Shi, J. Fripp, and P. Bourgeat, "Ea-GANs: Edge-aware generative adversarial networks for cross-modality MR image synthesis," *IEEE Transactions on Medical Imaging*, vol. 38, no. 7, pp. 1750–1762, 2019.
- [41] A. Sharma and G. Hamarneh, "Missing MRI pulse sequence synthesis using multi-modal generative adversarial network," *IEEE Transactions on Medical Imaging*, vol. 39, pp. 1170–1183, 2020.
- [42] G. Wang, E. Gong, S. Banerjee, D. Martin, E. Tong, J. Choi, H. Chen, M. Wintermark *et al.*, "Synthesize high-quality multi-contrast magnetic resonance imaging from multi-echo acquisition using multi-task deep generative model," *IEEE Transactions on Medical Imaging*, vol. 39, no. 10, pp. 3089–3099, 2020.
- [43] P. Isola, J.-Y. Zhu, T. Zhou, and A. A. Efros, "Image-to-image translation with conditional adversarial networks," *Proceedings of CVPR*, pp. 1125–1134, 2017.
- [44] J.-Y. Zhu, T. Park, P. Isola, and A. A. Efros, "Unpaired image-to-image translation using cycle-consistent adversarial networks," *Proceedings of ICCV*, pp. 2242–2251, 2017.
- [45] X. Wang, R. Girshick, A. Gupta, and K. He, "Non-local neural networks," in *Proceedings of CVPR*, 2018, pp. 7794–7803.
- [46] N. Kodali, J. Hays, J. Abernethy, and Z. Kira, "On convergence and stability of GANs," *arXiv:1705.07215*, 2017.
- [47] A. Dosovitskiy, L. Beyer, A. Kolesnikov, D. Weissenborn, X. Zhai, T. Unterthiner, M. Dehghani, M. Minderer *et al.*, "An image is worth 16x16 words: Transformers for image recognition at scale," *arXiv:2010.11929*, 2021.
- [48] J. Chen, Y. Lu, Q. Yu, X. Luo, E. Adeli, Y. Wang, L. Lu, A. L. Yuille *et al.*, "Transunet: Transformers make strong encoders for medical image segmentation," *arXiv:2102.04306*, 2021.
- [49] K. He, X. Zhang, S. Ren, and J. Sun, "Deep residual learning for image recognition," in *Proceedings of CVPR*, 2016, pp. 770–778.
- [50] X. Yi, E. Walia, and P. Babyn, "Generative adversarial network in medical imaging: A review," *Medical Image Analysis*, vol. 58, p. 101552, 2019.
- [51] G. Litjens, T. Kooi, B. E. Bejnordi, A. A. A. Setio, F. Ciompi, M. Ghafoorian, J. A. van der Laak, B. van Ginneken *et al.*, "A survey on deep learning in medical image analysis," *Medical Image Analysis*, vol. 42, pp. 60–88, 2017.
- [52] R. Li, W. Zhang, H.-I. Suk, L. Wang, J. Li, D. Shen, and S. Ji, "Deep learning based imaging data completion for improved brain disease diagnosis," in *MICCAI*. Springer, 2014, pp. 305–312.
- [53] A. Torrado-Carvajal, J. L. Herraiz, E. Alcain, A. S. Montemayor, L. García-Cañamaque, J. A. Hernandez-Tamames, Y. Rozenholc, and N. Malpica, "Fast patch-based pseudo-CT synthesis from t1-weighted MR images for PET/MR attenuation correction in brain studies," *Journal of Nuclear Medicine*, vol. 57, no. 1, pp. 136–143, 2016.
- [54] K. Bahrami, F. Shi, I. Reikik, and D. Shen, "Convolutional neural network for reconstruction of 7T-like images from 3T MRI using appearance and anatomical features," in *Deep Learning and Data Labeling for Medical Applications*. Springer, 2016, pp. 39–47.
- [55] K. Bahrami, F. Shi, X. Zong, H. W. Shin, H. An, and D. Shen, "Reconstruction of 7T-like images from 3T MRI," *IEEE Transactions on Medical Imaging*, vol. 35, no. 9, pp. 2085–2097, 2016.
- [56] Y. Zhang, P.-T. Yap, L. Qu, J.-Z. Cheng, and D. Shen, "Dual-domain convolutional neural networks for improving structural information in 3T MRI," *Magnetic Resonance Imaging*, vol. 64, pp. 90–100, 2019, artificial Intelligence in MRI.
- [57] X. Han, "MR-based synthetic CT generation using a deep convolutional neural network method," *Medical Physics*, vol. 44, no. 4, pp. 1408–1419, 2017.
- [58] D. Nie, X. Cao, Y. Gao, L. Wang, and D. Shen, "Estimating CT image from MRI data using 3D fully convolutional networks," in *Deep Learning and Data Labeling for Medical Applications*. Springer, 2016, pp. 170–178.
- [59] H. Arabi, G. Zeng, G. Zheng, and H. Zaidi, "Novel deep learning-based CT synthesis algorithm for MRI-guided PET attenuation correction in brain PET/MR imaging," in *Proceedings of IEEE NSS/MIC*, 2018, pp. 1–3.
- [60] K. Klaser, T. Varsavsky, P. Markiewicz, T. Vercauteren, D. Atkinson, K. Thielemans, B. Hutton, M. J. Cardoso *et al.*, "Improved MR to CT synthesis for PET/MR attenuation correction using imitation learning," in *Simulation and Synthesis in Medical Imaging*. Springer, 2019, pp. 13–21.
- [61] M. Mirza and S. Osindero, "Conditional generative adversarial nets," *arXiv:1411.1784*, 2014.
- [62] V. Sandfort, K. Yan, P. Pickhardt, and R. Summers, "Data augmentation using generative adversarial networks (cycleGAN) to improve generalizability in CT segmentation tasks," *Scientific Reports*, vol. 9, 11 2019.
- [63] M. Frid-Adar, I. Diamant, E. Klang, M. Amitai, J. Goldberger, and H. Greenspan, "GAN-based synthetic medical image augmentation for increased cnn performance in liver lesion classification," *Neurocomputing*, vol. 321, pp. 321–331, 2018.
- [64] A. Ben-Cohen, E. Klang, S. Raskin, S. Soffer, S. Ben-Haim, E. Konen, M. Amitai, and H. Greenspan, "Cross-modality synthesis from CT to PET using FCN and GAN networks for improved automated lesion detection," *Engineering Applications of Artificial Intelligence*, vol. 78, 2018.
- [65] G. Santini, C. Fourcade, N. Moreau, C. Rousseau, L. Ferrer, M. Lacombe, V. Fleury, M. Campone *et al.*, "Unpaired PET/CT image synthesis of liver region using CycleGAN," in *International Symposium on Medical Information Processing and Analysis*, vol. 11583, 2020, pp. 247 – 257.
- [66] C.-B. Jin, H. Kim, M. Liu, W. Jung, S. Joo, E. Park, Y. S. Ahn, I. H. Han *et al.*, "Deep CT to MR synthesis using paired and unpaired data," *Sensors*, vol. 19, no. 10, p. 2361, 2019.
- [67] Y. Ge, D. Wei, Z. Xue, Q. Wang, X. Zhou, Y. Zhan, and S. Liao, "Unpaired MR to CT synthesis with explicit structural constrained adversarial learning," in *Proceedings of IEEE ISBI*, 2019, pp. 1096–1099.
- [68] J. Wolterink, A. M. Dinkla, M. Savenije, P. Seevinck, C. Berg, and I. Isgum, "Deep MR to CT synthesis using unpaired data," in *Simulation and Synthesis in Medical Imaging*, 2017, pp. 14–23.
- [69] X. Dong, T. Wang, Y. Lei, K. Higgins, T. Liu, W. Curran, H. Mao, J. Nye *et al.*, "Synthetic CT generation from non-attenuation corrected PET images for whole-body PET imaging," *Physics in Medicine and Biology*, vol. 64, no. 21, p. 215016, 2019.
- [70] H. Yang, J. Sun, A. Carass, C. Zhao, J. Lee, Z. Xu, and J. Prince, "Unpaired brain MR-to-CT synthesis using a structure-constrained cycleGAN," *arXiv:1809.04536*, 2018.
- [71] Y. Hiasa, Y. Otake, M. Takao, T. Matsuoka, K. Takashima, A. Carass, J. Prince, N. Sugano *et al.*, "Cross-modality image synthesis from unpaired data using cyclegan: Effects of gradient consistency loss and training data size," in *Simulation and Synthesis in Medical Imaging*. Springer, 2018, pp. 31–41.
- [72] A. Chatsias, T. Joyce, R. Dharmakumar, and S. A. Tsiftaris, "Adversarial image synthesis for unpaired multi-modal cardiac data," in *Simulation and Synthesis in Medical Imaging*. Springer, 2017, pp. 3–13.
- [73] H. Do, P. Bourdon, D. Helbert, M. Naudin, and R. Guillemin, "7T MRI super-resolution with generative adversarial network," in *IST Electronic Imaging 2021 Symposium*, 2021.
- [74] L. Xiang, Y. Li, W. Lin, Q. Wang, and D. Shen, "Unpaired deep cross-modality synthesis with fast training," in *Deep Learning in Medical Image Analysis and Multimodal Learning for Clinical Decision Support*. Springer, 2018, pp. 155–164.
- [75] V. Kearney, B. P. Ziemer, A. Perry, T. Wang, J. W. Chan, L. Ma, O. Morin, S. S. Yom *et al.*, "Attention-aware discrimination for MR-to-CT image translation using cycle-consistent generative adversarial networks," *Radiology: Artificial Intelligence*, vol. 2, no. 2, p. e190027, 2020.
- [76] H. Zhang, I. Goodfellow, D. Metaxas, and A. Odena, "Self-attention generative adversarial networks," in *Proceedings of ICML*, ser. Proceedings of Machine Learning Research, K. Chaudhuri and R. Salakhutdinov, Eds., vol. 97, 2019, pp. 7354–7363.
- [77] O. Oktay, J. Schlemper, L. L. Folgoc, M. J. Lee, M. Heinrich, K. Misawa, K. Mori, S. G. McDonagh *et al.*, "Attention u-net: Learning where to look for the pancreas," *arXiv:1804.03999*, 2018.
- [78] J. Zhao, D. Li, Z. Kassam, J. Howey, J. Chong, B. Chen, and S. Li, "Tripartite-GAN: Synthesizing liver contrast-enhanced MRI to improve tumor detection," *Medical Image Analysis*, vol. 63, p. 101667, 2020.
- [79] Z. Yuan, M. Jiang, Y. Wang, B. Wei, Y. Li, P. Wang, W. Menpes-Smith, Z. Niu *et al.*, "Sara-GAN: Self-attention and relative average discriminator based generative adversarial networks for fast compressed sensing MRI reconstruction," *Frontiers in Neuroinformatics*, vol. 14, p. 58, 2020.
- [80] M. Li, W. Hsu, X. Xie, J. Cong, and W. Gao, "Saccn: Self-attention convolutional neural network for low-dose CT denoising with self-supervised perceptual loss network," *IEEE Transactions on Medical Imaging*, vol. 39, no. 7, pp. 2289–2301, 2020.
- [81] Y. Xie, J. Zhang, C. Shen, and Y. Xia, "Cotr: Efficiently bridging cnn and transformer for 3d medical image segmentation," *arXiv:2103.03024*, 2021.
- [82] D. Karimi, S. Vasylychko, and A. Gholipour, "Convolution-free medical image segmentation using transformers," *arXiv:2102.13645*, 2021.
- [83] Y. Dai and Y. Gao, "Transmed: Transformers advance multi-modal medical image classification," *arXiv:2103.05940*, 2021.
- [84] S. A. Kamran, K. F. Hossain, A. Tavakkoli, S. L. Zuckerbrod, K. M. Sanders, and S. A. Baker, "ViGAN: Semi-supervised retinal image synthesis and disease prediction using vision transformers," *arXiv:2104.06757*, 2021.
- [85] H.-C. Shin, A. Ihsani, S. Mandava, S. T. Sreenivas, C. Forster, J. Cha, and A. D. N. Initiative, "GANbert: Generative adversarial networks with bidirectional encoder representations from transformers for MRI to PET synthesis," *arXiv:2008.04393*, 2020.

- [86] X. Zhang, X. He, J. Guo, N. Etehad, N. Aw, D. Semanek, J. Posner, A. Laine *et al.*, “Ptnet: A high-resolution infant MRI synthesizer based on transformer,” *arXiv:2105.13993*, 2021.
- [87] A. Vaswani, N. M. Shazeer, N. Parmar, J. Uszkoreit, L. Jones, A. N. Gomez, L. Kaiser, and I. Polosukhin, “Attention is all you need,” *Proceedings of NIPS*, pp. 1–11, 2017.
- [88] S. Haykin, *Neural networks: a comprehensive foundation*. Prentice Hall PTR, 1994.
- [89] J. Ba, J. R. Kiros, and G. E. Hinton, “Layer normalization,” *ArXiv*, vol. abs/1607.06450, 2016.
- [90] B. H. Menze, A. Jakab, S. Bauer, J. Kalpathy-Cramer, and *et al.*, “The multimodal brain tumor image segmentation benchmark (brats),” *IEEE Transactions on Medical Imaging*, vol. 34, no. 10, pp. 1993–2024, 2015.
- [91] S. Bakas, H. Akbari, A. Sotiras, M. Bilello, M. Rozycki, J. Kirby, J. Freymann, K. Farahani *et al.*, “Advancing the cancer genome atlas glioma MRI collections with expert segmentation labels and radiomic features,” *Nature Scientific Data*, vol. 4, p. 170117, 2017.
- [92] S. Bakas, M. Reyes, A. Jakab, S. Bauer, M. Rempfler, A. Crimi, R. T. Shinohara, C. Berger *et al.*, “Identifying the best machine learning algorithms for brain tumor segmentation, progression assessment, and overall survival prediction in the brats challenge,” *arXiv:1811.02629*, 2019.
- [93] T. Nyholm, S. Svensson, S. Andersson, J. Jonsson, M. Sohlén, C. Gustafsson, E. Kjellén, K. Söderström *et al.*, “MR and CT data with multiobserver delineations of organs in the pelvic area—part of the gold atlas project,” *Medical Physics*, vol. 45, no. 3, pp. 1295–1300, 2018.
- [94] D. P. Kingma and J. Ba, “Adam: A method for stochastic optimization,” in *Proceedings of ICLR*, Y. Bengio and Y. LeCun, Eds., 2015.
- [95] T. Ridnik, E. Ben-Baruch, A. Noy, and L. Zelnik-Manor, “Imagenet-21k pretraining for the masses,” *arXiv:2104.10972*, 2021.
- [96] Z. Wang, A. Bovik, H. Sheikh, and E. Simoncelli, “Image quality assessment: From error visibility to structural similarity,” *IEEE Transactions on Image Processing*, vol. 13, pp. 600 – 612, 2004.
- [97] M. Heusel, H. Ramsauer, T. Unterthiner, B. Nessler, and S. Hochreiter, “GANs trained by a two time-scale update rule converge to a local nash equilibrium,” in *Proceedings of NIPS*, 2017, p. 6629–6640.
- [98] M. Yurt, S. U. H. Dar, M. Özbey, B. Tınaz, K. K. Oğuz, and T. Çukur, “Semi-supervised learning of mutually accelerated MRI synthesis without fully-sampled ground truths,” *arXiv:2011.14347*, 2021.
- [99] M. Jenkinson and S. Smith, “A global optimisation method for robust affine registration of brain images,” *Medical Image Analysis*, vol. 5, pp. 143–156, 2001.
- [100] H. Lan, the Alzheimer Disease Neuroimaging Initiative, A. W. Toga, and F. Sepehrband, “Three-dimensional self-attention conditional GAN with spectral normalization for multimodal neuroimaging synthesis,” *Magnetic Resonance in Medicine*, vol. 86, no. 3, pp. 1718–1733, 2021.
- [101] S. Abnar and W. Zuidema, “Quantifying attention flow in transformers,” *Proceedings of ACL*, pp. 4190–4197, 2020.
- [102] Z. Wojna, V. Ferrari, S. Guadarrama, N. Silberman, L. Chieh Chen, A. Fathi, and J. Uijlings, “The devil is in the decoder: Classification, regression and GANs,” *International Journal of Computer Vision*, vol. 11-12, 2019.
- [103] R. Durall, M. Keuper, and J. Keuper, “Watch your up-convolution: Cnn based generative deep neural networks are failing to reproduce spectral distributions,” in *Proceedings of CVPR*, 2020, pp. 7887–7896.

## SUPPLEMENTARY MATERIALS

### VII. SUPPLEMENTARY TEXT

#### A. Datasets

1) *IXI Dataset*:  $T_1$ -weighted,  $T_2$ -weighted, and PD-weighted brain MR images from 53 healthy subjects were analyzed. 25 subjects were reserved for training, 10 were reserved for validation, and 18 were reserved for testing. From each subject, 100 axial cross-sections containing brain tissues were selected. Acquisition parameters were as follows.  $T_1$ -weighted images:  $TE = 4.603ms$ ,  $TR = 9.813ms$ , spatial resolution =  $0.94 \times 0.94 \times 1.2mm^3$ .  $T_2$ -weighted images:  $TE = 100ms$ ,  $TR = 8178.34ms$ , spatial resolution =  $0.94 \times 0.94 \times 1.2mm^3$ . PD-weighted images:  $TE = 8ms$ ,  $TR = 8178.34ms$ , spatial resolution =  $0.94 \times 0.94 \times 1.2mm^3$ . The multi-contrast images in this dataset were unregistered. Hence,  $T_2$ - and PD-weighted images were spatially registered onto  $T_1$ -weighted images prior to modelling. Registration was performed via an affine transformation in FSL [99] based on mutual information.

2) *BRATS Dataset*:  $T_1$ -weighted,  $T_2$ -weighted, post-contrast  $T_2$ -weighted, and  $T_2$  Fluid Attenuation Inversion Recovery (FLAIR) brain MR images from 55 subjects were analyzed. 25 subjects were reserved for training, 10 were reserved for validation, and 20 were reserved for testing. From each subject, 100 axial cross-sections containing brain tissues were selected. Please note that the BRATS dataset contains images collected under various clinical protocols and scanners at multiple institutions. As publicly shared, multi-contrast images are co-registered to the same anatomical template, interpolated to  $1 \times 1 \times 1mm^3$  resolution and skull-stripped.

3) *MRI-CT Dataset*:  $T_2$ -weighted MR and CT images of the male pelvis from 15 subjects were used. 9 subjects were reserved for training, 2 were reserved for validation, and 4 were reserved for testing. From each subject, 90 axial cross-sections were analysed. Acquisition parameters were as follows.  $T_2$ -weighted MR images: Group 1,  $TE = 97ms$ ,  $TR = 6000-6600ms$ , spatial resolution =  $0.875 \times 0.875 \times 2.5mm^3$ . Group 2,  $TE = 91 - 102ms$ ,  $TR = 12000 - 16000ms$ , spatial resolution =  $0.875 - 1.1 \times 0.875 - 1.1 \times 2.5mm^3$ . CT images: Group 1, spatial resolution =  $0.98 \times 0.98 \times 3mm^3$ , Kernel =  $B30f$ . Group 2: spatial resolution =  $0.1 \times 0.1 \times 2mm^3$ , Kernel =  $FC17$ . This MRI-CT dataset contains images collected under various different protocols and scanners for each modality. As publicly shared, multi-modal images are co-registered onto  $T_2$ -weighted MR scans.



## B. Competing Methods

### 1) Convolutional models:

**pGAN:** A convolutional GAN model, pGAN, with ResNet backbone was considered [24]. pGAN comprises CNN-based generator and discriminator networks [24]. Its generator comprises an encoder, bottleneck, and decoder, where the encoder and decoder are identical to those in ResViT. The bottleneck contains a cascade of 9 residual CNN blocks. Note that pGAN receives as input a specific collection of source modality images to synthesize target modality images in one-to-one or many-to-one settings, so a separate pGAN model was trained independently for each distinct synthesis task.

**pix2pix:** A convolutional GAN model, pix2pix, with U-Net backbone was considered [43]. The CNN-based pix2pix has a generator with an encoder-decoder structure tied with skip connections [43]. An independent pix2pix model was learned for each distinct synthesis task.

**MM-GAN:** A unified synthesis model based on a convolutional GAN architecture was considered [41]. MM-GAN comprises CNN-based generator and discriminator networks, where the generator is based on U-Net. MM-GAN trains a single network under various source-target modality configurations. The original MM-GAN architecture was directly adopted, except for curriculum learning to ensure standard sample selection for all competing methods. The unification strategy in MM-GAN matches the unification strategy in ResViT.

**pGAN<sub>uni</sub>:** A unified version of the pGAN model was trained to consolidate multiple synthesis tasks. The unification procedure was identical to that of ResViT.

### 2) Attention-augmented convolutional models:

**Attention U-Net (A-UNet):** A CNN-based U-Net architecture with additive attention gates was considered [77]. Here we adopted the original A-UNet model as the generator of a conditional GAN model, where the discriminator was identical to that in ResViT.

**Self-Attention GAN (SAGAN):** A CNN-based GAN model with self-attention modules incorporated into the generator was considered [76]. Here we adapted the original SAGAN model designed for unconditional mapping by inserting the self-attention modules into the pGAN model as described in [100]. For a fair comparison, the number and position of attention modules in SAGAN were matched to those of transformer modules in ResViT. A separate SAGAN model was learned for each distinct synthesis task.

### 3) Transformer models:

**TransUNet:** A hybrid CNN-transformer architecture, TransUNet [48], recently introduced for medical image segmentation, was considered. Here, we adopted the original TransUNet model as the generator of a conditional GAN architecture with an identical discriminator to ResViT. We further replaced the segmentation head with a convolutional layer for synthesis. A separate TransUNet model was trained for each distinct synthesis task.

**TransUNet<sub>uni</sub>:** The TransUNet model was unified to consolidate multiple synthesis tasks. The unification procedure was identical to that of ResViT.

### C. Architectural Details

The encoder in the ResViT model contained three convolutional layers of kernel size 7, 3, 3 respectively. The feature map in the encoder output was of size  $\mathbb{R}^{256,64,64}$ , and this dimensionality was retained across the information bottleneck. The decoder contained three convolutional layers of kernel size 3, 3, 7 respectively. The information bottleneck contained nine ART blocks. The downsampling modules preceding transformers contained two convolutional layers with stride 2 and kernel size 3. The upsampling modules succeeding transformers contained two transposed convolutional layers with stride 2 and kernel size 3. Down and upsampling factors were set to  $M = 4$ . Channel compression lowered the number of channels from 512 to 256. Patch flattening was performed with size  $P = 1$  corresponding to  $\mathbb{R}^{16 \times 16}$  patches in the original images [47].

Note that transformer modules contain substantially higher number of parameters compared to convolutional modules. Thus, retaining a transformer in each ART block results in significant model complexity, inducing computational burden and suboptimal learning. To alleviate these issues, transformer modules in ART blocks utilized tied weights. Furthermore, they were only retained in a subset of ART blocks, while remaining blocks reduced to residual CNNs.

The configuration of transformer modules, i.e. their total number and position, was selected via cross-validation experiments. Due to the extensive number of potential configurations, a pre-selection process was implemented. Accordingly, performance for a transformer module inserted in a single ART block ( $A_1, A_2, \dots, A_9$ ) was measured, and the top half of positions was pre-selected. Composite configurations with multiple transformer modules were then formed based on the pre-selected blocks ( $A_1 - A_5, A_1 - A_6 - A_9$  etc.). We observed that retaining more than 2 modules elevated complexity without any performance benefits. Validation performance for the best performing configurations ( $A_1 - A_5, A_1 - A_6, A_1 - A_9, A_5 - A_9, A_4 - A_9, A_5 - A_9, A_1 - A_6 - A_9$ ) are listed in Supp. Table I for three representative tasks ( $T_1, T_2 \rightarrow \text{PD}$  in IXI,  $T_1, T_2 \rightarrow \text{FLAIR}$  in BRATS, and  $\text{MRI} \rightarrow \text{CT}$  in MRI-CT). Consistently across tasks, the ( $A_1 - A_6$ ) configuration yielded near-optimal performance and so it was selected for all experiments thereafter.

We also tuned the intrinsic complexity of transformer modules. To do this, two variant modules were examined: "base" and "large". The "base" module contained 12 layers with latent dimensionality  $N_d = 768$ , 12 attention heads, and 3073 hidden units in each layer of the MLP. Meanwhile, the "large" module contained 24 layers with latent dimensionality  $N_d = 1024$ , 16 attention heads and 4096 hidden units in each layer of the MLP. Validation performances based on the two variant modules are listed in Supp. Table II. The "base" module that offers higher performance for lower computational complexity was selected for consequent experiments.

#### D. Ablation Studies

ResViT leverages a synergistic combination of residual convolutional modules and transformer modules in ART blocks, as well as adversarial learning. First, controlled experiments were performed to assess the contribution of each component to model performance. To do this, separate models were trained where each component was individually removed. Specifically, variant models were trained when transformer modules were ablated from the respective ART blocks, when residual CNNs were ablated from transformer-retaining ART blocks, and when adversarial learning was turned off by ablating the discriminator subnetwork. Here, in order to assess the importance of adversarial learning, we additionally measured the Fréchet inception distance (FID) [97] between the synthesized and ground truth images for ResViT and ablated models.

Second, we examined the importance of the architectural design of ART blocks in ResViT. Controlled experiments were conducted to assess the benefit of using tied versus untied weights across transformer modules and using two versus single transformer-retaining ART blocks. To do this, variant models were trained separately using untied weights in transformers, and based on a single transformer-retraining module at either first or sixth ART blocks.

Third, we assessed the importance of training strategies in enhancing model convergence for the ResViT model. Here we proposed to initiate transformer modules in ResViT with versions pre-trained on ImageNet. We also performed delayed insertion of the transformer modules into the model during training. To assess the contributions of these strategies, three variant models were built where randomly initialized transformer modules were used, where pre-trained transformer modules were inserted into ART blocks at the beginning of training, and where randomly initialized transformer modules were inserted at the beginning of training.

To interpret the information that self-attention mechanisms focus on during synthesis tasks, we computed and visualized the attention maps as captured by the transformer modules in ResViT. Attention maps were calculated based on the Attention Rollout technique, and a single average map was extracted for a given transformer module [101].

### *E. ResViT versus TransUNet*

Superior depiction of pathology in ResViT signals the importance of aggregated transformer blocks in simultaneously maintaining local precision and contextual consistency in medical image synthesis. Although TransUNet also employs a transformer to capture context, it yields suboptimal synthesis quality in various tasks. This performance loss might be associated with two fundamental differences between the models. First, TransUNet forces CNN-based feature maps from its encoder through a transformer, while it uses skip connections to propagate only shallow convolutional features from earlier layers. ResViT instead continues encoding and propagating convolutional features across the information bottleneck, creating a much deeper and better-distilled feature representation. Importantly, residual skip connections within ART blocks are critical to ResViT’s performance, as we have observed in our validation studies. Second, the decoder in TransUNet performs bilinear upsampling to progressively increase the spatial resolution of synthesized images [48]. Several prior studies have suggested that bilinear interpolation might be suboptimal in suppressing high-frequency artifacts [102], [103]. In ResViT, we employ transposed convolutions within the upsampler modules in ART blocks and within the decoder to mitigate potential artifacts.



## VIII. SUPPLEMENTARY TABLES

**Supp. Table I:** Validation performance of candidate ResViT configurations in representative synthesis tasks. Performance is taken as PSNR (dB) between synthesized and reference target images.  $A_i$  denotes the presence of a transformer module in the  $i$ th ART block.

Configuration	$T_1, T_2 \rightarrow PD$	$T_1, T_2 \rightarrow FLAIR$	$MRI \rightarrow CT$
	PSNR	PSNR	PSNR
$A_1 - A_5$	33.23	24.82	26.40
$A_1 - A_6$	<b>33.34</b>	<b>24.88</b>	26.56
$A_1 - A_9$	33.27	24.77	<b>26.58</b>
$A_4 - A_9$	33.11	24.63	26.19
$A_5 - A_9$	33.05	24.65	26.27
$A_1 - A_6 - A_9$	32.89	24.82	26.20

**Supp. Table II:** Validation performance of ResViT models with varying sizes of transformer modules in representative synthesis tasks.

Transformer size	$T_1, T_2 \rightarrow PD$	$T_1, T_2 \rightarrow FLAIR$	$MRI \rightarrow CT$
	PSNR	PSNR	PSNR
Base	<b>33.34</b>	<b>24.88</b>	<b>26.56</b>
Large	33.14	24.60	26.46

**Supp. Table III:** Average inference times of synthesis models per single cross-section. Compute times are reported for processing on a single nVidia RTX A4000 GPU.

	ResViT	pGAN	pix2pix	A-UNet	SAGAN	TransUNet
Inference (msec)	98	60	60	70	63	78

**Supp. Table IV:** Performance of task-specific synthesis models in one-to-one tasks ( $T_2 \rightarrow PD$  and  $PD \rightarrow T_2$ ) in the IXI dataset. PSNR (dB) and SSIM (%) measurements are listed as mean $\pm$ std across test subjects. Boldface indicates the model with the top performance for a given task.

		ResViT	pGAN	pix2pix	A-UNet	SAGAN	TransUNet
$T_2 \rightarrow PD$	PSNR	<b>32.90</b>	32.20	30.72	32.05	32.07	30.90
		$\pm 1.20$	$\pm 1.00$	$\pm 1.28$	$\pm 1.04$	$\pm 0.98$	$\pm 1.35$
	SSIM	<b>0.972</b>	0.963	0.956	0.960	0.963	0.960
		$\pm 0.005$	$\pm 0.005$	$\pm 0.007$	$\pm 0.009$	$\pm 0.006$	$\pm 0.006$
$PD \rightarrow T_2$	PSNR	<b>34.24</b>	33.05	30.74	33.32	32.96	31.73
		$\pm 1.09$	$\pm 0.95$	$\pm 1.63$	$\pm 1.08$	$\pm 1.01$	$\pm 1.44$
	SSIM	<b>0.972</b>	0.963	0.950	0.961	0.962	0.958
		$\pm 0.005$	$\pm 0.007$	$\pm 0.012$	$\pm 0.007$	$\pm 0.007$	$\pm 0.008$

**Supp. Table V:** Performance of task-specific synthesis models in one-to-one tasks ( $T_2 \rightarrow \text{FLAIR}$  and  $\text{FLAIR} \rightarrow T_2$ ) in the BRATS dataset. PSNR (dB) and SSIM (%) measurements are listed as mean $\pm$  std across test subjects. Boldface indicates the model with the top performance for a given task.

		ResViT	pGAN	pix2pix	A-UNet	SAGAN	TransUNet
$T_2 \rightarrow \text{FLAIR}$	PSNR	<b>24.97</b>	24.01	23.15	23.69	24.02	23.70
		$\pm 1.07$	$\pm 1.15$	$\pm 1.93$	$\pm 1.57$	$\pm 1.35$	$\pm 1.75$
	SSIM	0.870	0.864	0.869	<b>0.873</b>	0.860	0.864
		$\pm 0.014$	$\pm 0.014$	$\pm 0.016$	$\pm 0.015$	$\pm 0.015$	$\pm 0.015$
$\text{FLAIR} \rightarrow T_2$	PSNR	<b>25.78</b>	25.09	24.52	24.56	25.10	24.62
		$\pm 0.92$	$\pm 1.52$	$\pm 0.88$	$\pm 0.94$	$\pm 0.88$	$\pm 0.81$
	SSIM	<b>0.908</b>	0.894	0.883	0.891	0.893	0.891
		$\pm 0.015$	$\pm 0.015$	$\pm 0.014$	$\pm 0.014$	$\pm 0.014$	$\pm 0.015$

**Supp. Table VI:** Performance of ResViT and ablated variants in three representative synthesis tasks. Ablations were performed for transformer modules, convolutional modules and adversarial training. PSNR (dB) and SSIM (%) are listed as mean $\pm$ std across test subjects. Note that FID is a summary metric across the entire test set. Boldface indicates the model with the top performance for a given task.

	$T_1, T_2 \rightarrow \text{PD}$			$T_1, T_2 \rightarrow \text{FLAIR}$			$\text{MRI} \rightarrow \text{CT}$		
	PSNR	SSIM	FID	PSNR	SSIM	FID	PSNR	SSIM	FID
ResViT	<b>33.92</b>	<b>0.977</b>	<b>14.47</b>	<b>25.84</b>	0.886	<b>18.58</b>	28.45	<b>0.932</b>	60.28
	$\pm 1.44$	$\pm 0.004$		$\pm 1.13$	$\pm 0.014$		$\pm 1.35$	$\pm 0.009$	
w/o transformers	32.91	0.966	14.56	24.96	0.868	19.21	26.73	0.899	95.38
	$\pm 0.96$	$\pm 0.005$		$\pm 1.10$	$\pm 0.005$		$\pm 0.91$	$\pm 0.008$	
w/o residual CNN	33.49	0.971	14.84	25.11	0.874	20.30	28.19	0.922	<b>60.16</b>
	$\pm 1.34$	$\pm 0.005$		$\pm 1.02$	$\pm 0.014$		$\pm 1.15$	$\pm 0.009$	
w/o adversarial loss	33.75	0.977	15.80	22.95	<b>0.891</b>	40.68	<b>28.58</b>	0.932	65.49
	$\pm 1.45$	$\pm 0.005$		$\pm 1.93$	$\pm 0.015$		$\pm 1.13$	$\pm 0.007$	

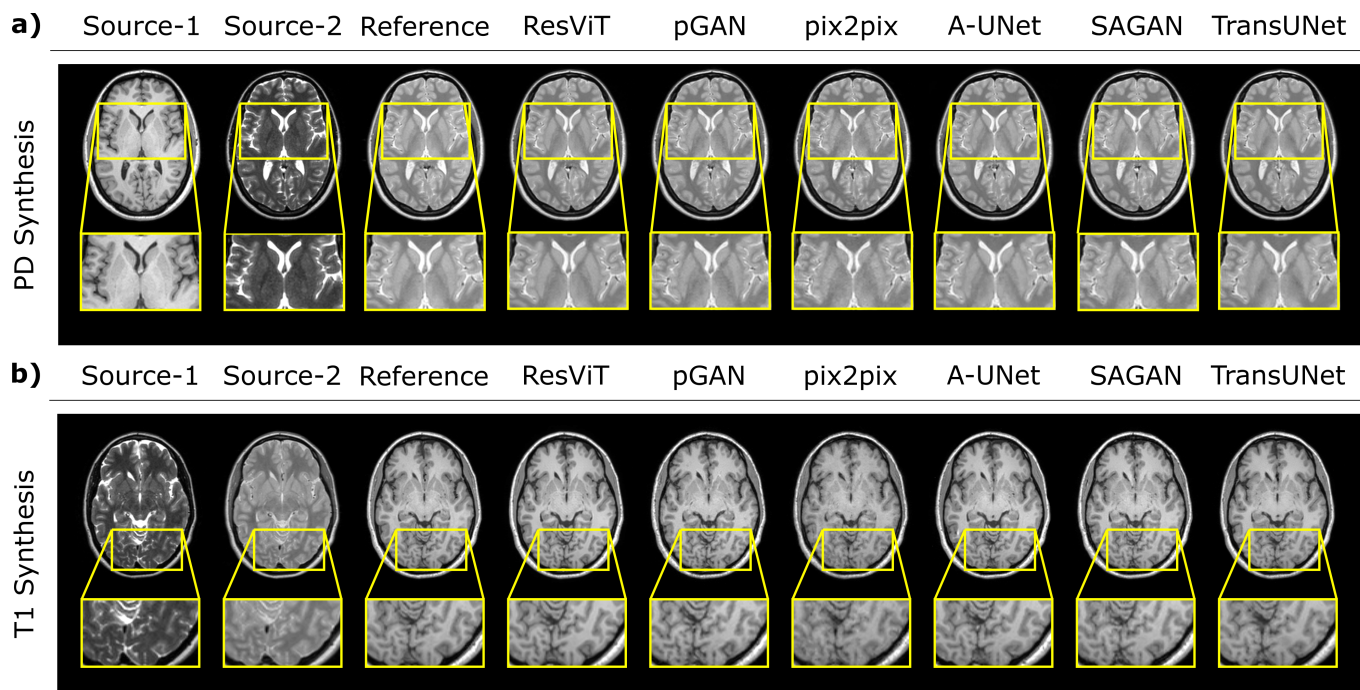
**Supp. Table VII:** Performance of ResViT and ablated variants in three representative synthesis tasks. Ablations were performed for weight tying, and individual transformer modules. PSNR (dB) and SSIM (%) are listed as mean $\pm$ std across test subjects. Boldface indicates the model with the top performance for a given task.

	$T_1, T_2 \rightarrow \text{PD}$		$T_1, T_2 \rightarrow \text{FLAIR}$		$\text{MRI} \rightarrow \text{CT}$	
	PSNR	SSIM	PSNR	SSIM	PSNR	SSIM
$A_1 - A_6$	<b>33.92</b>	<b>0.977</b>	<b>25.84</b>	<b>0.886</b>	<b>28.45</b>	<b>0.931</b>
	$\pm 1.44$	$\pm 0.004$	$\pm 1.13$	$\pm 0.014$	$\pm 1.35$	$\pm 0.009$
$A_1 - A_6$ (untied weights)	33.72	0.973	25.19	0.879	28.16	0.923
	$\pm 1.23$	$\pm 0.005$	$\pm 1.18$	$\pm 0.014$	$\pm 1.11$	$\pm 0.007$
$A_1$	33.51	0.971	24.98	0.883	28.06	0.921
	$\pm 1.15$	$\pm 0.005$	$\pm 1.60$	$\pm 0.015$	$\pm 1.31$	$\pm 0.008$
$A_6$	33.78	0.977	25.25	0.880	27.95	0.921
	$\pm 1.34$	$\pm 0.004$	$\pm 1.20$	$\pm 0.014$	$\pm 1.22$	$\pm 0.008$

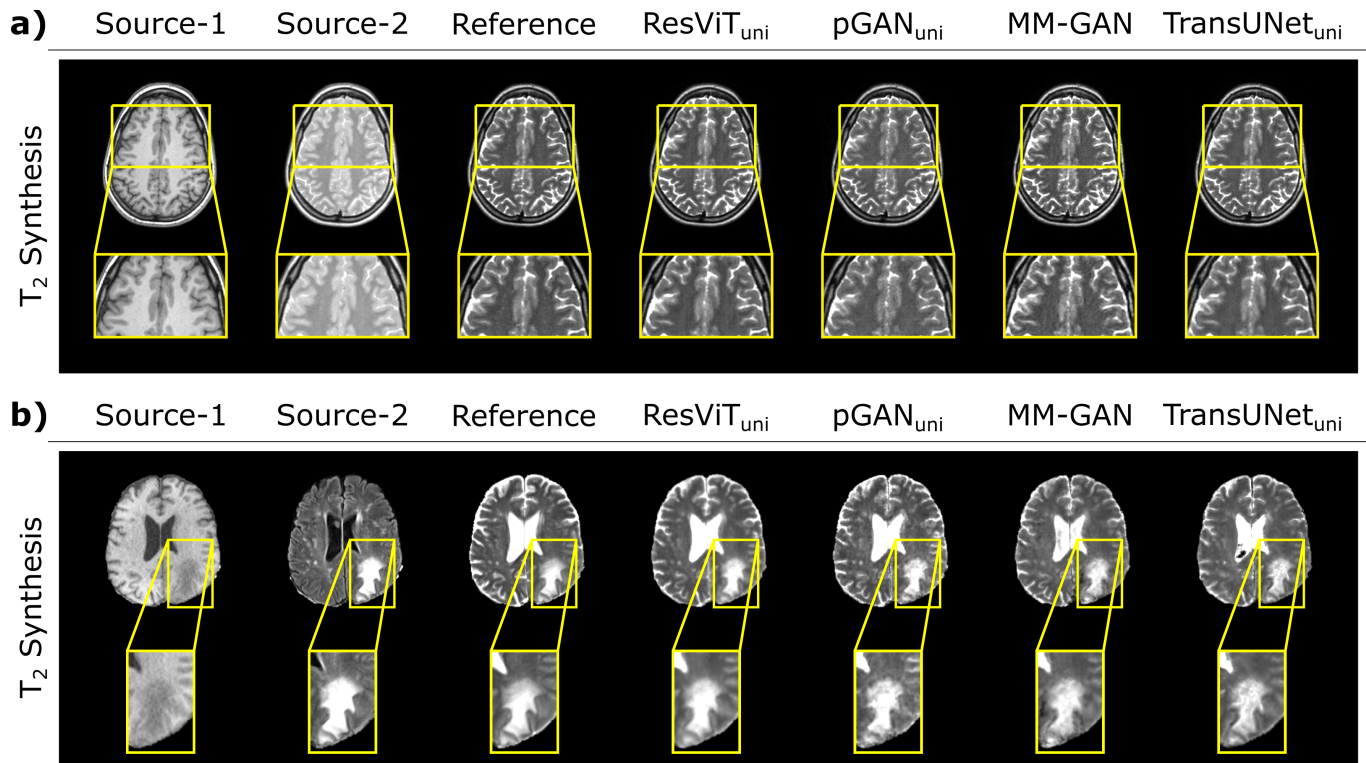
**Supp. Table VIII:** Performance of ResViT and ablated variants in three representative synthesis tasks. Variant models were built by ablating transformer pre-training (i.e. randomly initialized transformer), delayed insertion of transformers (i.e. inserted into the model at the beginning of training), and both transformer pretraining and delayed insertion. PSNR (dB) and SSIM (%) are listed as mean $\pm$ std across test subjects. Boldface indicates the model with the top performance for a given task.

	$T_1, T_2 \rightarrow \text{PD}$		$T_1, T_2 \rightarrow \text{FLAIR}$		$\text{MRI} \rightarrow \text{CT}$	
	PSNR	SSIM	PSNR	SSIM	PSNR	SSIM
ResViT	<b>33.92</b>	<b>0.977</b>	<b>25.84</b>	<b>0.886</b>	<b>28.45</b>	<b>0.931</b>
	$\pm 1.44$	$\pm 0.004$	$\pm 1.13$	$\pm 0.014$	$\pm 1.35$	$\pm 0.009$
w/o transformer pre-training	33.55	0.971	24.86	0.881	27.94	0.922
	$\pm 1.25$	$\pm 0.005$	$\pm 1.28$	$\pm 0.016$	$\pm 1.25$	$\pm 0.009$
w/o delayed insertion	33.35	0.977	24.89	0.873	28.01	0.924
	$\pm 1.13$	$\pm 0.004$	$\pm 1.18$	$\pm 0.015$	$\pm 1.27$	$\pm 0.008$
w/o transformer pre-training or delayed insertion	33.58	0.971	24.74	0.869	27.66	0.913
	$\pm 1.16$	$\pm 0.005$	$\pm 1.30$	$\pm 0.016$	$\pm 0.78$	$\pm 0.006$

## IX. SUPPLEMENTARY FIGURES

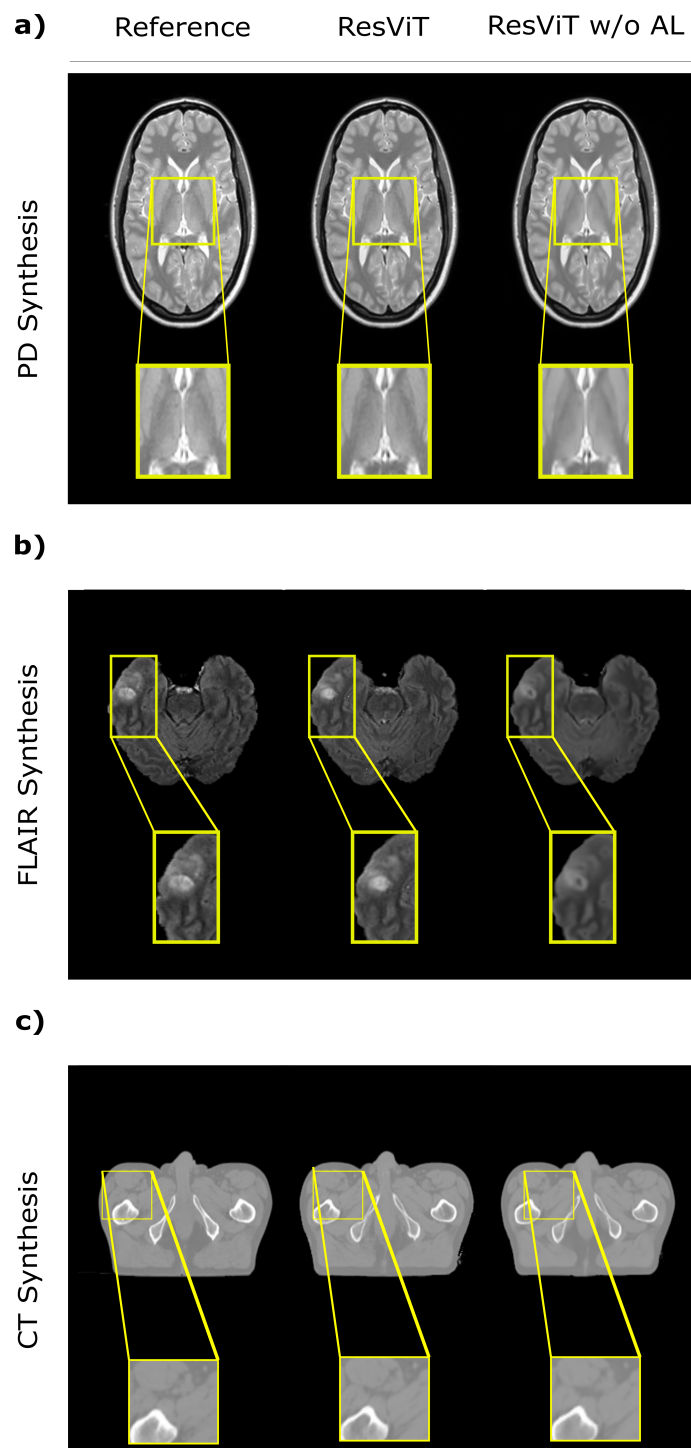


**Supp. Fig. 1:** ResViT was demonstrated on the IXI dataset for two representative many-to-one synthesis tasks: a)  $T_1, T_2 \rightarrow PD$ , b)  $T_2, PD \rightarrow T_1$ . Synthesized images from all competing methods are shown along with the source images and the reference target image. ResViT improves synthesis performance in regions that are depicted sub-optimally in competing methods. Overall, ResViT generates images with lower artifact and noise levels and sharper tissue depiction.

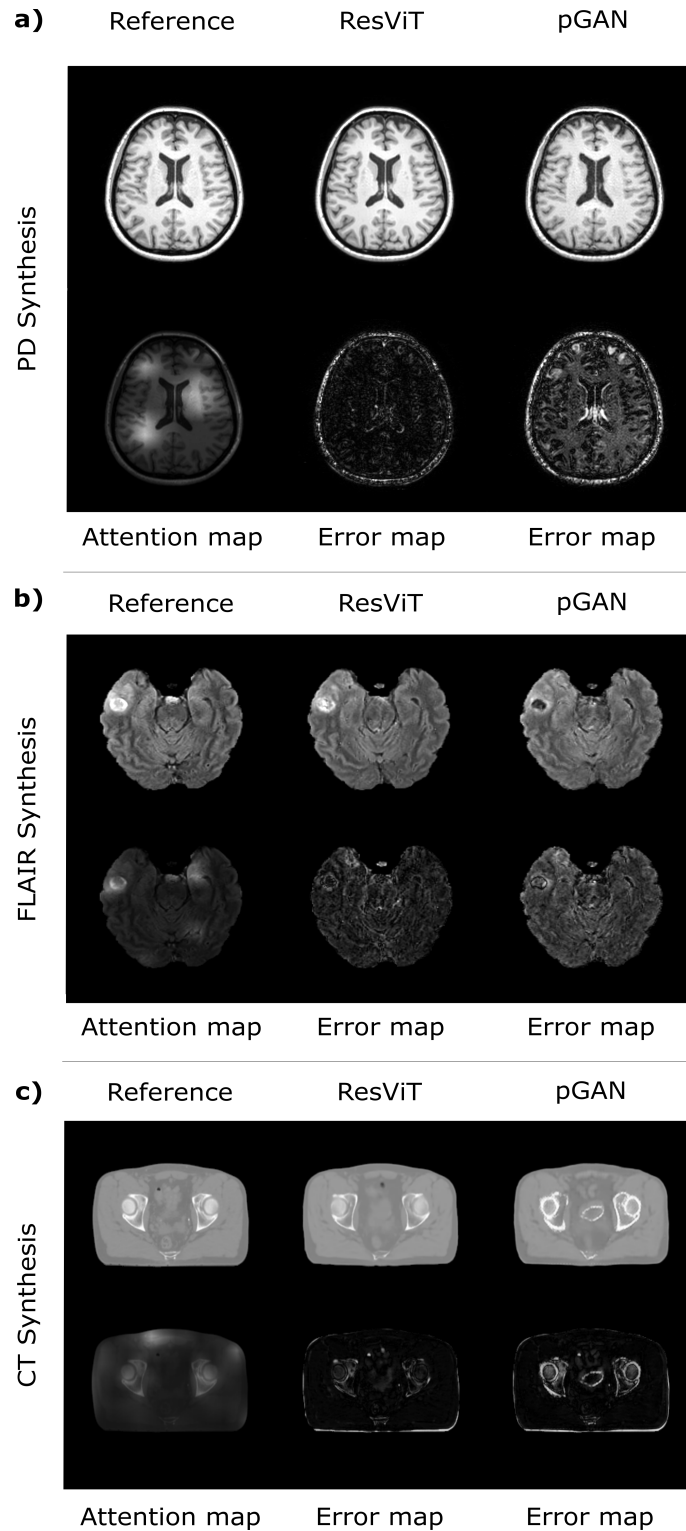


**Supp. Fig. 2:** ResViT<sub>uni</sub> was demonstrated against other unified models on brain MRI datasets for two representative tasks: a) T<sub>1</sub>, PD → T<sub>2</sub> in IXI, b) T<sub>1</sub>, FLAIR → T<sub>2</sub> in BRATS. Synthesized images from all competing methods are shown along with the source images and the reference target image. ResViT<sub>uni</sub> improves synthesis performance especially in pathological regions (tumors, lesions) in comparison to competing methods. Overall, ResViT<sub>uni</sub> generates images with lower artifact and noise levels and more accurate tissue depiction for tasks in both datasets.





**Supp. Fig. 3:** ResViT was demonstrated against an ablated variant obtained by removing the adversarial term from the loss function (i.e., ablating the discriminator subnetwork). Representative results are shown for  $T_1, T_2 \rightarrow PD$  in IXI,  $T_1, T_2 \rightarrow FLAIR$  in BRATS, and  $MRI \rightarrow CT$  in the pelvic dataset. Synthesized images from the models are shown along with the reference images. Adversarial loss improves the acuity of synthesized images.



**Supp. Fig. 4:** Representative synthesis results from ResViT and pGAN are shown along with the reference images for  $T_2$ , PD  $\rightarrow$   $T_1$  in IXI,  $T_1$ ,  $T_2 \rightarrow$  FLAIR in BRATS, and MRI  $\rightarrow$  CT in the pelvic dataset. Error maps between the synthetic and reference images for each method are displayed, along with the attention map within the first transformer module of ResViT. Here, the attention maps were overlaid onto the reference image for improved visualization. Attention maps focus on image regions where ResViT substantially reduces synthesis errors compared to pGAN.